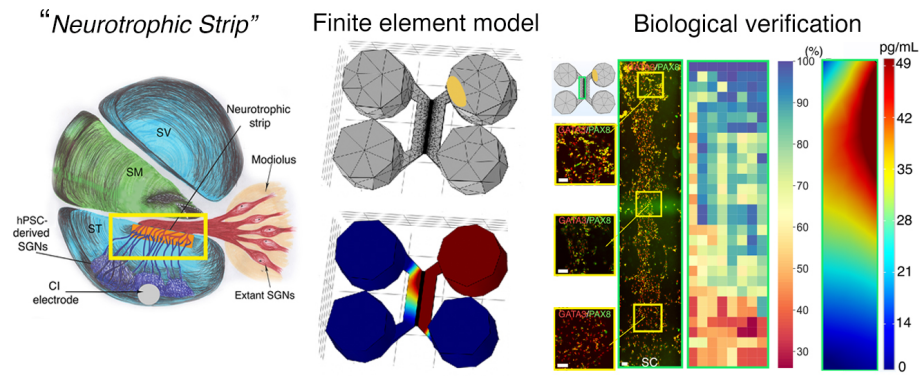


Graphical Abstract

Developing the Bioactive Cochlear Implant: Bridging the electrode–neuron gap through neurite guidance

Kevin T. Nella, Benjamin M. Norton, Hsiang-Tsun Chang, Rachel A. Heuer,
Christian B. Roque, Akihiro J. Matsuoka



Developing the Bioactive Cochlear Implant: Bridging the electrode–neuron gap through neurite guidance

Kevin T. Nella^{a,b}, Benjamin M. Norton^a, Hsiang-Tsun Chang^a, Rachel A. Heuer^a, Christian B. Roque^a, Akihiro J. Matsuoka^{a,c,d,e,*}

^a*Department of Otolaryngology–Head and Neck Surgery, Feinberg School of Medicine, Northwestern University, Chicago IL, 60611, USA*

^b*Department of Mechanical Engineering, Robert R. McCormick School of Engineering and Applied Science, Northwestern University, Evanston IL., 60208, USA*

^c*Simpson Querrey Institute, Chicago IL, 60611, USA*

^d*Roxelyn and Richard Pepper Department of Communication Sciences and Disorders, School of Communication, Northwestern University, Evanston, IL., 60201, USA*

^e*The Hugh Knowles Center for Clinical and Basic Science in Hearing and its Disorders, Evanston, IL. 60201, USA*

Abstract

Although cochlear implant (CI) technology has allowed for the partial restoration of hearing over the last few decades, persistent challenges, such as the translation of rich acoustic signals into digital pulse-train signals, remain. The “electrode–neuron gap” poses the most significant obstacle to advancing past the current plateau in CI performance. Resulting issues include poor performance in noisy environments and a limited ability to decode intonation and music. We propose the development of a “neuro-regenerative nexus”—a biological interface that doubly preserves endogenous spiral ganglion neurons (SGNs) while precisely directing the growth of neurites arising from transplanted human pluripotent stem cell (hPSC)-derived otic neuronal progenitors (ONPS) toward endogenous SGNs. We hypothesized that the Polyhedrin Delivery System (PODS®-human brain-derived neurotrophic factor (BDNF)) could stably

*Corresponding author: Akihiro J. Matsuoka, Department of Otolaryngology–Head and Neck Surgery, Feinberg School of Medicine, Northwestern University, 676 North St. Clair Street Suite 1325, Chicago, IL 60611, USA. E-mail addresses: amatsuok@nm.org, akihiro.matsuoka@northwestern.edu.

Email addresses: kevinnella2022@u.northwestern.edu (Kevin T. Nella), benjamin.norton@northwestern.edu (Benjamin M. Norton), hsiangtsun.chang@gmail.com (Hsiang-Tsun Chang), racheuer@gmail.com (Rachel A. Heuer), christian.b.roq@gmail.com (Christian B. Roque), amatsuok@nm.org (Akihiro J. Matsuoka)

provide an adequate BDNF concentration gradient to hPSC-derived ONPs and thereby facilitate otic neuronal differentiation and directional neurite outgrowth. To test this hypothesis, a finite element model was constructed in order to simulate the *in vitro* BDNF concentration gradient generated by PODS®. For biological validation, cell culture experiments were conducted using a multi-chamber microfluidic device that more closely mirrors the micro-environment of the inner ear than conventional laboratory plates, especially in terms of volume and concentrations of endogenous factors. We were able to generate the optimal BDNF concentration gradient to enable survival, neuronal differentiation toward SGNs, and directed neurite extension of hPSC-derived SGNs. The technique will allow us to further advance our concept of a “neuro-regenerative nexus” by controlling neurite direction of transplanted hPSC-derived ONPs and their endogenous counterparts. This proof-of-concept study provides a step toward the next generation of CI technology.

Keywords: human pluripotent stem cells, finite element model, microfluidic device, neurotrophic factor, cochlear implant, neuroelectric interface, stem cell niche, spiral ganglion neurons

2010 MSC: 74S05, 62P10, 92C20

¹ **1. Introduction**

² The cochlear implant (CI), which provides functional restoration in patients
³ with sensorineural hearing loss, forms a neuro-electronic interface with the au-
⁴ ditory nervous system [1]. CI technology functions by electrically stimulating
⁵ the extant population of auditory neurons (i.e., spiral ganglion neurons [SGNs]).
⁶ Although CI technology has allowed partial restoration of hearing for this pa-
⁷ tient population over the last few decades, persistent challenges, such as the
⁸ translation of rich acoustic signals into digital pulse-train signals, remain. Cen-
⁹ tral to many of these challenges, the “electrode-neuron gap” poses the most
¹⁰ significant obstacle to advancing past the current plateau in CI performance.
¹¹ This phenomenon symptomatically manifests as poor performance in noisy envi-
¹² ronments and a limited ability to decode intonation and music [2], consequently
¹³ associated with a decreased quality of life for many. The gap exists between CI
¹⁴ electrodes and target membranes of dendrites of surviving endogenous SGNs [3].
¹⁵ It results in the requirement of larger CI excitation fields, which lead to current
¹⁶ spread that excites and therefore disables neighboring electrodes, resulting in
¹⁷ fewer information channels to the brain [2, 4]. This develops into a vicious cycle
¹⁸ as fewer information channels to the brain require larger CI excitation fields.
¹⁹ The width of the gap generally spans hundreds of μm [5, 6]. Hahnewald et al.
²⁰ demonstrated *in vitro* that energy needed to elicit a response can be reduced by
²¹ up to 20% by decreasing the width from 40 to zero μm (early postnatal mouse
²² SGN explants were grown on a microelectrode array) [4].

²³ Previous work has introduced the concept of a ”bioactive” CI to resolve the
²⁴ electrode-neuron gap *in vivo*[7, 8, 9]. The bioactive CI combines current state-
²⁵ of-the-art CI technology with emerging stem cell-replacement therapy in the
²⁶ inner ear. In this scheme, transplanted human pluripotent stem cell (hPSC)-
²⁷ derived SGNs bridge the gap between the CI and surviving endogenous SGNs.
²⁸ However, the issue of establishing synaptic connections between the two cell
²⁹ populations remain.

³⁰ Neurotrophin gradients have been shown to guide hPSC grafts in spinal cord

31 injury [10], direct growth of endogenous SGNs toward CI electrodes in the scala
32 tympani [11], and enable transplanted hPSC-derived otic neuronal progenitors
33 (ONPs) to grow neurites toward the modiolus [9]. Although promising, these
34 studies failed to demonstrate adequate directed neurite outgrowth (e.g., lack of
35 synaptic connections between hPSC grafts and endogenous SGNs), presumably
36 precluding significant improvements in functional recovery of hearing.

37 To confront this issue, we propose the development of a “neuro-regenerative
38 nexus”—a bioengineered interface that doubly preserves endogenous SGNs and
39 precisely directs the growth of neurites arising from differentiated transplanted
40 hPSC-derived ONPs toward the endogenous SGNs, and vice versa. The high-
41 lighted yellow-square area in Figure 1A shows a schematic diagram of this con-
42 cept. Here, the neuro-regenerative nexus (shown as an orange rectangle) stimu-
43 lates directed neurite outgrowth from both hPSC-derived ONPs and endogenous
44 SGNs via a neurotrophic factor gradient [12]. While the concept of using neu-
45 rotrophin gradients for directional axonal growth has existed for a few decades,
46 implementation has been extremely challenging due to the lack of self-sustaining
47 neurotrophin delivery methods; their eventual depletion triggers an accelerated
48 decline in neurite growth and survival of extant SGNs [13, 14, 15]. One ma-
49 jor contributor is the biochemical instability of neurotrophins, which suffer from
50 structural fragility and thermo-instability under normal physiological conditions
51 both *in vitro* and *in vivo*, resulting in half-lives typically ranging from minutes to
52 hours [16]. We set out to mitigate this phenomenon by utilizing the polyhedrin
53 delivery system (PODS®)—a crystalline growth factor formulation developed
54 to facilitate extended release of growth factors (e.g., neurotrophins) [17, 18, 19]
55 (Figure 1B). The PODS® technology has adapted viral machinery to encase a
56 selected growth factor into polyhedrin protein crystals. The resultant growth
57 factor co-crystals have slow degradation profiles under physiological conditions
58 and, therefore, allow the sustained release of the embedded bioactive growth
59 factors.

60 We reasoned that a bio-engineered scaffolding integrated with PODS® tech-
61 nology can establish a neuronal network between transplanted hPSC-derived

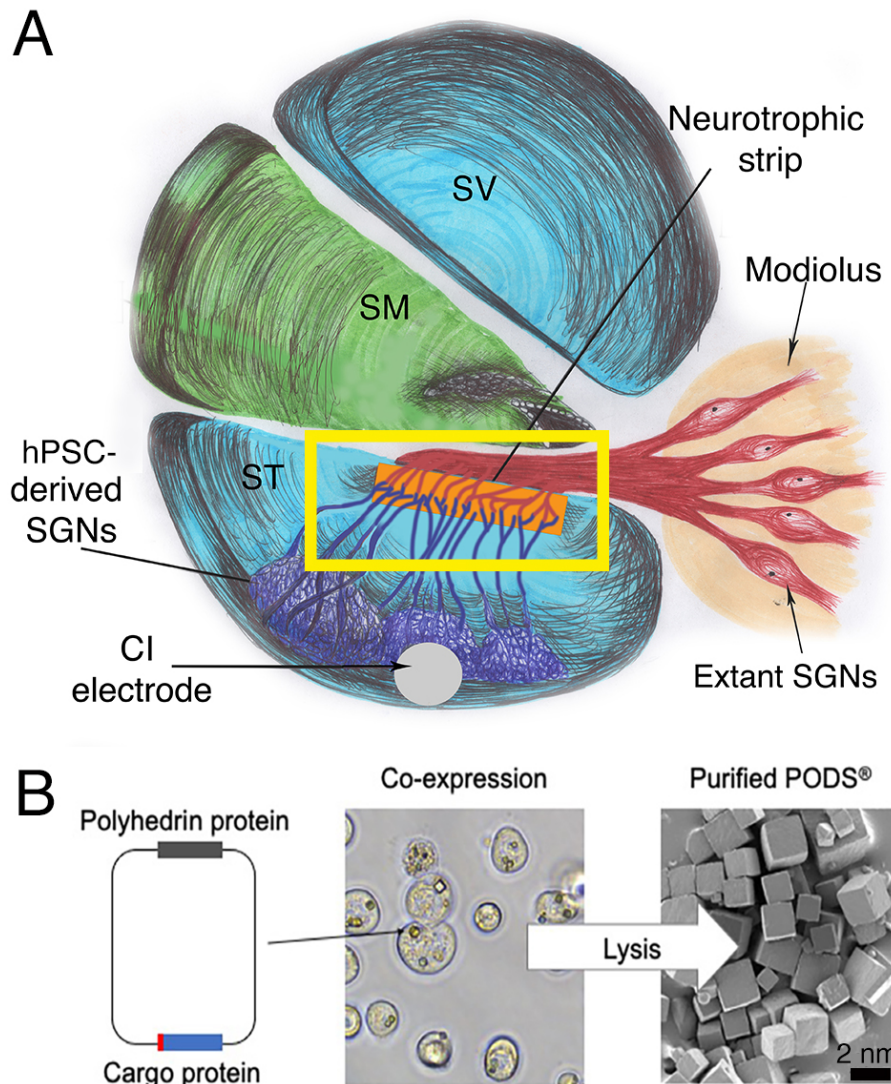


Figure 1: (A): A next-generation bioactive CI and the neuro-regenerative nexus. The neural network in this scheme consists of a CI, transplanted stem cell-derived SGNs, a neuro-regenerative nexus, and extant/endogenous SGNs (red). Note that neuronal connection is largely absent with hair cells (not shown). (B): Polyhedrin Delivery System (PODS)[®]. PODS[®] crystals are cubic protein co-crystals produced by Sf9 cells (a clonal isolate of *Spodoptera frugiperda* Sf21 cells [IPLB-Sf21-AE], in which the polyhedrin protein and a second “cargo” protein are co-expressed) (Figure 1B, left). Inside the Sf9 cells, polyhedrin proteins self-assemble into cubic crystals (Figure 1B, center) while the active protein, tagged with a short peptide sequence, binds to the growing polyhedrin crystal. The crystals are extracted and purified by simple cell lysis followed by washes to remove cell debris (Scanning electron micrograph, Figure 1B, right).

62 ONP grafts and extant SGNs in the inner ear. More specifically, we hypothe-
63 sized that PODS®-recombinant human neurotrophin system could stably pro-
64 vide and maintain an adequate neurotrophin gradient for the facilitation of
65 ONP differentiation and directional neurite outgrowth. To test this hypothesis,
66 we constructed a finite element model (FEM) to simulate the *in vitro* neu-
67 rotrophin concentration gradient generated by PODS®. In this study, we focus
68 on BDNF—the most studied of the neurotrophins in the inner ear, and the most
69 vital for functional recovery of damaged SGNs [20]. For biological validation we
70 employed a multi-chamber microfluidic device that more closely mirrors the *in*
71 *vivo* micro-environment of the inner ear than conventional laboratory plates in
72 terms of volume and concentrations of endogenous factors [21].

73 **2. Materials and Methods**

74 *2.1. Polyhedrin delivery system*

75 The Polyhedrin Delivery System (PODS®-recombinant human BDNF [rhBDNF])
76 (Cell Guidance Systems, Cambridge, United Kingdom) was used as the self-
77 sustaining source of rhBDNF. PODS®-rhBDNF is composed of the polyhedrin
78 protein formed by *Bombyx mori*, an insect from the moth family *Bombycidae*.
79 A cargo protein (i.e., rhBDNF) is co-expressed within the polyhedrin crystal
80 and is slowly released by breakdown of the PODS® crystals via cell-secreted
81 proteases (Figure 1B)[9, 18, 22].

82 *2.2. Enzyme-linked immunosorbent assay for brain-derived neurotrophic factor*

83 Concentrations of rhBDNF were measured at sequential time points to de-
84 termine the degradation and release kinetics of PODS®-rhBDNF crystals. Cul-
85 ture media from control and experimental conditions were collected at each time
86 point and immediately stored at -80°C. An enzyme-linked immunosorbent assay
87 (ELISA) was performed after the final collection. The same method was applied
88 to measure the degradation kinetics of rhBDNF protein with a carrier protein
89 (Bovine Serum Albumin [BSA]) (#248-BDB-050, R&D Systems, Minneapolis,

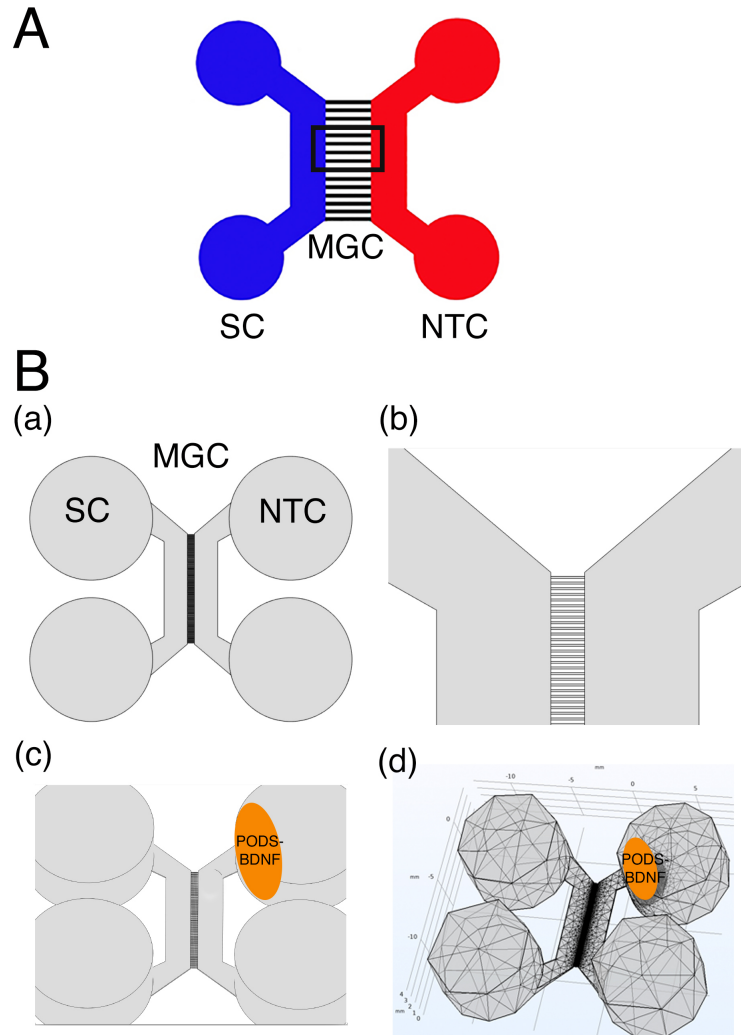


Figure 2: (A): Schematic representation of a Xona™ Microfluidics XC 450. Two main compartments (somal compartment (SC) and neurotrophin compartment (NTC)) on either side are connected by a micro-groove channel array (MGC) spanning 450 μm , each individual channel having a width of 10 μm (black square). The somal compartment contains hPSC-derived late-stage ONPs (shown in black), while the neurotrophin compartment largely contains the secreted factors (i.e., BDNF) that are released from the PODS®-rhBDNF crystals deposited in its upper well. (B):(a) Xona™ Microfluidics XC450 device geometry, created at a 1:1 scale with Autodesk Inventor®, in which the diffusion profile of the released BDNF was modeled. (b) Detail of the microchannels adjoining the two compartments of the Xona™ Microfluidics XC450. (c) Xona™ Microfluidics XC450 device showing the optimal location and geometry of the volume of PODS®-rhBDNF (yellow ellipse). (d): Mesh geometry of the Xona™ XC450 generated with Autodesk Inventor, depicting the localized volume of PODS®-rhBDNF (1 μL) as an ellipsoid disc.

90 Minnesota, USA). Experimental conditions were culture media enriched with
91 10% fetal bovine serum (FBS) (Thermo Fisher Scientific, Waltham, MA, USA).
92 All rhBDNF samples were quantified with a BDNF ELISA kit (# BGK23560;
93 PeproTech, Rocky Hill, New Jersey, USA), and the results were analyzed with
94 a Synergy HTX Multi-Mode Reader (BioTek, Winocski, Vermont, USA) at a
95 450 nm wavelength, as instructed by the manufacturer. Molecular kinetics were
96 then calculated using a self-coded curve fit analysis as well as the MATLAB
97 Curve Fitting Toolbox (MathWorks, Natick, CA, USA). These kinetics data
98 are consequential in the finite element model, to be described in a later section.

99 *2.3. Sodium dodecyl sulphate–polyacrylamide gel electrophoresis*

100 Sodium dodecyl-sulfate polyacrylamide gel electrophoresis (SDS-PAGE) was
101 used to formulate the molar ratio of polyhedrin to BDNF in PODS®-rhBDNF,
102 required for an exceptionally accurate finite element analysis, described in a
103 later section. SDS-PAGE is commonly used as a method to separate proteins
104 with molecular masses between 5 and 250 kDa [26], which is suitable for de-
105 tecting rhBDNF (molecular weight [MW]: 14kDa [27]) and polyhedrin (MW:
106 ~29 kDa [22]). Briefly, each protein sample was diluted in deionized water and
107 mixed with 6x Laemmli sample buffer (Bio-Rad Laboratories, Inc., Des Plaines,
108 Illinois [IL], USA) containing 2-mercaptoethanol and heated at 100°C for 5 to 20
109 minutes. Samples were then loaded into precast Mini-PROTEAN TGX 4-15%
110 polyacrylamide mini-gels (Bio-Rad Laboratories, Inc., Des Plaines, IL, USA).
111 Then, 5 mL of Precision Plus Protein Kaleidoscope Prestained Protein Stan-
112 dards (Bio-Rad Laboratories, Inc., Des Plaines, IL, USA) were loaded in each gel
113 run. Electrophoresis was performed at room temperature for approximately 90
114 minutes using a constant voltage (100V) in 1x solution of Tris-Glycine-SDS elec-
115 trophoresis buffer (Bio-Rad Laboratories, Inc., Des Plaines, IL, USA) until the
116 dye front reached the end of the 60 mm gel. After electrophoresis, the mini-gels
117 were rinsed with deionized water 3 times for 5 minutes and were subsequently
118 incubated in SimplyBlue™ SafeStain (ThermoFisher Scientific, Waltham, MA,
119 USA) for one hour at room temperature with gentle agitation. Images ob-

tained from gels were analyzed using ImageJ 1.53g (December 4, 2020, the National Institutes of Health, Bethesda, MD, USA [28]). The calculated molar ratio from the analysis was applied to the COMSOL® Multiphysics model to accurately predict the rhBDNF concentration gradient arising from PODS®-rhBDNF. SDS-PAGE was performed according to the manufacturer's technical guide (Bio-Rad Laboratories, Inc., Des Plaines, IL, USA).

2.4. Western Blot

The identity of the rhBDNF protein detected by SDS-PAGE was confirmed by Western blot (Bio-Rad Laboratories, Inc., Des Plaines, IL, USA). The polyvinylidene difluoride (PVDF) membrane was prepared in methanol for 30 seconds before soaking in 1x Tris-Glycine-Methanol transfer buffer for 10 minutes. Wet transfer was performed at 4°C for approximately 60 minutes using a constant voltage (100V) in 1X solution of Tris-Glycine-Methanol transfer buffer. After transfer, the membrane was briefly rinsed with 1X Tris-buffered saline Tween-20 (TBST) and was subsequently blocked in 5% BSA in TBST for 24 hours at 4°C with gentle agitation. The membrane was then rinsed with 1x TBST before incubating with BDNF polyclonal antibody (ThermoFisher Scientific, Waltham, MA, USA) diluted to 1:1500 in 1% BSA in TBST for 24 hours at 4°C with gentle agitation. Following incubation, the membrane was rinsed in 1x TBST 5 times for 5 minutes to remove unbound primary antibody. Next, the membrane was incubated in Goat anti-Rabbit IgG (H+L) horseradish peroxidase (HRP) conjugated secondary antibody (ThermoFisher Scientific, Waltham, MA, USA) diluted to 1:5000 in 1% BSA in TBST for one hour at room temperature with gentle agitation. Following incubation, the membrane was rinsed in 1x TBST 5 times for 5 minutes to remove unbound secondary antibody. For sensitive detection, the membrane was treated with Pierce™ ECL Western Blotting Substrate (ThermoFisher Scientific, Waltham, MA, USA), and visualized using an Azure 600 Digital Imager (Azure Biosystems, Dublin, CA, USA). Electrophoresis buffer for sample condition and run condition was summarized in Supplementary Table S1.

150 *2.5. Three-dimensional finite element analysis*

151 We used finite element analysis (FEA) to simulate the BDNF concentration
152 gradient over time in a multi-chamber microfluidic device. FEA is a compu-
153 tational numerical technique, which approximates mathematical solutions to
154 partial differential equations (PDEs) that appropriately simulate complex real-
155 world problems including stress/strain testing, thermal conduction, and mass
156 transport in various geometries and materials. In this study, the FEM allowed
157 us to predict the concentration gradient with respect to time depending on the
158 quantity of PODS®-rhBDNF introduced into the system. To solve the FEM,
159 we used COMSOL® Multiphysics (version 5.6 [released on November 11, 2020],
160 COMSOL, Inc., Burlington, Massachusetts [MA], USA), which is a finite ele-
161 ment method solution tool for engineering and scientific research computations.
162 We used sustained-release kinetics for PODS®-rhBDNF determined from afore-
163 mentioned ELISA and SDS-PAGE experiments, as well as data from a previous
164 study by our group [9]. Device geometry was constructed at a 1:1 scale us-
165 ing Autodesk® Inventor 2019.0.2 (Autodesk, Mill Valley, CA, USA) (Figure
166 3B). The FEA was computed with a high-performance desktop computer plat-
167 form equipped with a 64 GB RAM CPU (AMD Ryzen Threadripper 3990X
168 64-Core, 128-Thread @ 4.3 GHz) and two GPU cards (NVIDIA GeForce RTX
169 3080Ti,12GB 384-bit GFF6X Graphics card).

170 *2.6. Human pluripotent stem cell culture using dual-compartment microfluidic
171 device*

172 Human embryonic stem cells (hESCs: H7 and H9, passage number 25–35)
173 were obtained from WiCell Research Institute (Madison, Wisconsin, USA). Hu-
174 man induced pluripotent stem cells (hiPSCs: TC-1133HKK, passage number
175 22–35) were generated from human CD34+ cord blood cells using the four
176 Yamanaka factors at Lonza (Walkersville, Maryland [MD], USA). The hiPSC
177 cell line (TC-1133HKK) was kindly provided by Healios K.K. (Tokyo, Japan).
178 hPSC-derived ONPs were generated based on our previously established proto-
179 col (Supplemental Data) [8, 9, 23, 24]. A step-wise series of ligands and growth

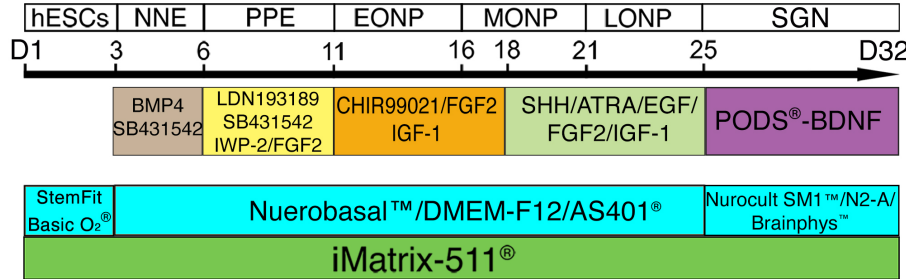


Figure 3: Overview of otic neuronal differentiation protocol for hPSCs. Please see detail in [8, 9, 23, 24] and the Supplemental Data. Each developmental stage is shown at the top, with key treatments shown below. NNE: nonneuronal ectoderm; PPE: preplacodal ectoderm; EONP: early-stage otic neuronal progenitor; MONP: mid-stage otic neuronal progenitor; LONP: late-stage otic neuronal progenitor; BMP4: bone morphogenetic protein 4; SHH: Sonic hedgehog; ATRA: all-trans retinoic acid; EGF: epidermal growth factor; IGF-1: insulin-like growth factor-1; FGF2: fibroblast growth factor 2; N2B27-CDM: chemically defined medium containing N2 and B27 supplements.

180 factors was added to the neuronal induction medium to promote hPSC differentiation toward the late-stage ONP lineage—the mitotic progenitor population 181 that generates SGNs. (Figure 3).

183 Microfluidic devices provided a platform for specifically evaluating axonal 184 regeneration [25]. Here, multi-chamber microfluidic devices, Xona™ Microfluidics 185 XC150 and XC450 (Xona™ Microfluidics, Research Triangle Park, North 186 Carolina, USA), were used in computational modeling and biological validation 187 (Figure 3A–B) of the FEA. The Xona™ device allows for neurites to grow toward 188 growth factors in the opposite chamber while limiting migration of derived 189 ONP cell bodies due to specific dimensions of the device. The microchannel array 190 between the two chambers also mirrors the porous bony separation (osseous 191 spiral lamina) between the modiolus (where extant SGNs are localized) and the 192 scala tympani (where the biohybrid CI is implanted) [41, 42].

193 The devices were washed and coated with poly-L-ornithine (PLO, 20 µg/mL 194 in H₂O, Sigma-Aldrich, St. Louis, Missouri [MO], USA) and recombinant 195 laminin-511 (iMatrix-511, 0.5 mg/mL, Nacalai USA, San Diego, California [CA],

196 USA) according to the manufacturer-outlined protocol. Next, approximately
197 1.75×10^5 cells (in 20 μL of media) were plated in the somal compartment
198 through the top and bottom left wells (i.e., total amount of 3.5×10^5 hPSC-
199 derived ONPs were added).

200 A specified quantity of PODS®-rhBDNF crystals were deposited in the top
201 right well of the neurotrophin compartment (Figure 3A–B). hPSC-derived ONPs
202 were cultured for 7 days in the Xona™ device to induce otic neuronal differen-
203 tiation and neurite growth. Note that high-density cell cultures were induced
204 to facilitate molecular studies as well as the generation of a more biologically
205 relevant neuronal phenotype (i.e., otic lineage) [25]. Media was topped off daily
206 after imaging (from 20–40 μL per well). Experiments were done in three biolog-
207 ical replicates unless otherwise specified in Figure captions.

208 *2.7. Immunocytochemistry and image acquisition*

209 On Day 7, 4% (w/v) paraformaldehyde (PFA) (ThermoFisher Scientific,
210 Waltham, MA, USA) was added to the compartments for 20 minutes to fix the
211 cells. Immunocytochemistry was used to assess GATA3, PAX8, and beta-III
212 tubulin expression. These three proteins were shown to appropriately charac-
213 terize ONPs in our previous studies [8, 9, 24]. Following PBS washes, cultures
214 were blocked with 5% BSA at room temperature for 1 hour. Cultures were then
215 incubated overnight at 4°C on a shaker plate in primary antibody solution us-
216 ing Rabbit anti-Beta-III-Tubulin (1:100, Abcam, Cambridge, MA, USA), Goat
217 anti-PAX8 (1:500, Abcam, Cambridge, MA, USA), and Mouse anti-GATA3
218 (1:500, R&D Systems, Minneapolis, MN, USA). Following PBS washes, cultures
219 were incubated at room temperature for 90 minutes on a shaker plate in sec-
220 ondary antibody solution composed of Alexafluor647 anti-Rabbit (1:1000, Ther-
221 moFisher Scientific, St. Louis, MO, USA), Alexafluor488 anti-Goat (1:1000,
222 ThermoFisher Scientific, St. Louis, MO, USA), and Alexafluor594 anti-Mouse
223 (1:1000, ThermoFisher Scientific, St. Louis, MO, USA) in 1% BSA. Follow-
224 ing PBS washes, cultures were incubated with DAPI for 20 minutes (300 nM,
225 ThermoFisher Scientific, St. Louis, MO, USA). Secondary antibody controls

were performed each time multiple primary antibodies were used [29]. Labeling controls (detection controls) were performed for a sample from each hPSC culture [29]. See Supplementary Figure S1 for exemplary figures for these control conditions. Results were imaged using a Nikon Ti2 Widefield Laser Microscope System (Nikon, Tokyo, Japan). Phase-contrast images were captured on a Nikon Eclipse TE2000-U inverted microscope (Nikon, Tokyo, Japan). All fluorescence images were acquired on a Zeiss LSM 510 META laser-scanning confocal microscope (Carl Zeiss, Oberkochen, Germany), a Nikon Ti2 laser laser-scanning confocal microscope (Nikon, Tokyo, Japan), or a Leica SP5 laser-scanning confocal microscope (Leica, Welzlar, Germany). Observers were blinded to the conditions during imaging and tracing. In general, the images were processed in ImageJ ver. 1.53g or Matlab R2020b. Further detail on image acquisition and quantification of fluorescent-positive cells can be found in the Supplemental Data.

2.8. Preferred cell orientation analysis

Collective cell migration, where cells organized in a tightly connected fashion migrate as cohesive structures, is a critical biological process to highlight the neurotrophin diffusion profile [30]. To evaluate this process, time-lapse acquisition of images of the Xona™ device was performed using an inverted microscope (Nikon Eclipse TS100, Tokyo, Japan) on days 1, 3, 5, and 7. Due to the high cell density required for hPSC-derived late stage ONPs to survive in the somal compartment of the Xona™ device, images were not amenable to manual analysis in most of the cases. To circumvent this problem, we performed a series of image pre-processings that are mainly based on modified binarization-based extraction of alinement score methods with some modifications [31]. We used MATLAB Image Processing Toolbox R2020b (version 9.9.0.1495850, September 30th, 2020, Mathworks, Natick, MA) for analysis. Please see Supplementary Figure S2 for further detail. The analysis of directional data in general represents a particular challenge: there is no reason to designate any particular point on the circle as zero, and it is somewhat arbitrary depending on where one sets a coordinate

[32, 33]. In this study, we used polar coordinates to determine the directionality of preferred cell orientation. For this analysis, we again used MATLAB Image Processing Toolbox R2020b. See detailed discussion on how we determined the preferred cell orientation in Supplementary Figure S3.

2.9. Neurite alignment vector assay, neurite growth assay and cell migration assay

The microfluidic device allowed us to culture hPSC-derived ONPs in a polarized manner and to directly isolate/analyze neurites. To evaluate neurite projection into the neurotrophin compartment by derived otic neurons cultured in the somal compartment, we performed a neurite alignment vector assay. We also evaluated the length of neurites that grew from hPSC-derived ONPs. For these purposes, hPSC-derived ONPs were cultured in a Xona™ XC450 for seven days and were then immunostained with *beta*-III tubulin and DAPI. We used two ImageJ plug-in toolkits, NeuriteTracer and NeuronJ, to assess neurite alignment and neurite growth [34, 35]. Due to the bipolar nature of hPSC-derived ONPs/SGNs, we measured the two longest neurites from each cell [24, 36]. Please see Supplementary Figure S4 for detailed description of this analysis. We used hPSC-derived ONPs cultured with 800,000 PODS®-rhBDNF crystals as a positive control. This quantity was selected based on our FEM in that concentrations were so high that there was no biologically relevant concentration gradient. As a negative control, we used 20 ng/mL of recombinant human BDNF (standard culture condition). To evaluate cell migration across the microgroove channels, we performed cell migration analysis. We manually counted the number of ONPs that migrated from the somal compartment into the microchannels and neurotrophin compartment.

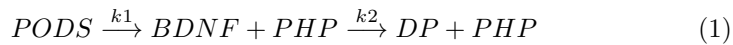
2.10. Statistical analysis

When appropriate, and as indicated in each figure, statistical analysis was performed. Experimental values are typically expressed as mean and standard error (SE). The majority of the statistical analyses were performed with Python

3.9.6. (Python Software Foundation, Wilmington, Delaware, USA). The following libraries were used for the statistical analysis: Scipy, Numpy, Matplotlib, and Seaborn [37, 38, 39]. Normal distributions were assumed unless otherwise mentioned. P values smaller than 0.05 were considered statistically significant. For circular statistics, we derived the sample mean vector and its polar coordinate. Mean and confidence intervals were calculated. We chose confidence coefficient, Q (e.g. $Q = 0.95$). To analyze the axial nature of the data, especially to compute the mean vector angle, we doubled each angle and reduced the multiples modulo 360° . Please see detailed discussion in Supplementary Figure S3 and S5. Rayleigh test of uniformity and V-test were performed to determine whether the samples differ significantly from randomness (i.e., where there is statistical evidence of directionality). One-sample test for the mean angle was performed to test whether the population mean angle is statistically different from the given angle. In all of our circular statistics, von Mises distribution was assumed and also verified. Circular statistics were performed using CircStat: A MATLAB Toolbox [33, 40]. Please see detailed description of circular statistics in Supplementary Figure S3 and S5.

3. Results

The appropriate quantity of PODS[®]-rhBDNF crystals to induce an effective neurotrophin gradient for otic neuronal differentiation and directed neurite outgrowth was derived using a three-dimensional FEA that predicts the concentration profile of BDNF formed through the gradual release and diffusion of BDNF from PODS[®]-rhBDNF. First, we quantified the molecular kinetics of this phenomenon with ELISA testing (Figure 4) to establish parameters for the FEA. Here, two consecutive molecular reactions occur: 1) the breakdown of PODS[®] crystals into polyhedrin protein and rhBDNF, and 2) the degradation of rhBDNF towards the degradation product (Equation (1)).



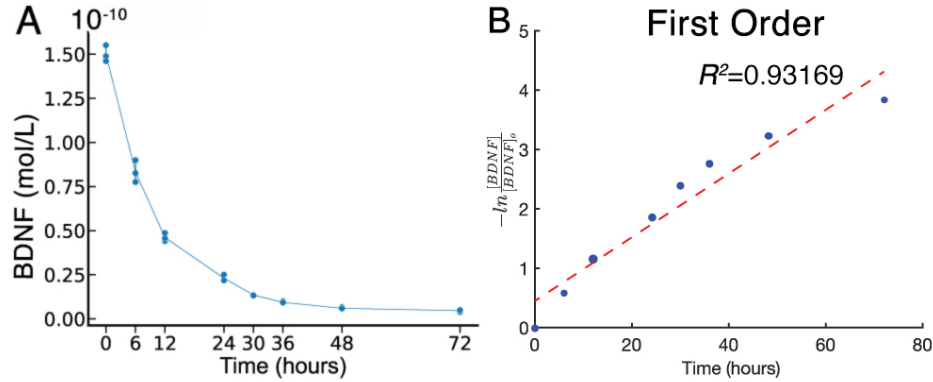


Figure 4: Chemical kinetics of Brain Derived Neurotrophic Factor (BDNF). (A): Concentration of rhBDNF in solution over 72 hours after initial application. (B): $\frac{1}{[BDNF]}$ data fit to first order curve. Please see other curve fit data in Supplemental Figure 1. Red line: fitted line, blue dots: individual data point. k_2 is defined as slope of fitted curve.

where DP is the degradation product of the released rhBDNF, PHP is the polyhedrin protein, and k_1 and k_2 are the rate constants ($\frac{1}{hour}$) for their respective reactions.

Degradation kinetics data for rhBDNF were collected while monitoring rhBDNF concentration after introducing a predefined amount into a single well of solution. The data obtained throughout the first 72 hours indicate an exponential decay, suggesting first-order kinetics (Figure 4). To confirm this interpretation, we performed linear and nonlinear least square analyses of the kinetics data with the MATLAB Curve Fitting Toolbox. We found that the corresponding R^2 for the first-order curve-fit was 0.93169, confirming that rhBDNF degradation in the experimental condition is indeed first-order. The rate constant for a first-order reaction is defined to be the slope of the semi-logarithmic plot of measured concentration (proportional to initial concentration) vs time. The value for k_2 is calculated to be 0.0679 ($\frac{1}{hour}$) (See further detail in Supplementary Figure S7). Furthermore, data for the complete molecular reaction were collected by similarly monitoring rhBDNF concentration over time after placing a predefined quantity of PODS®-rhBDNF crystals into a single well of solution. The data

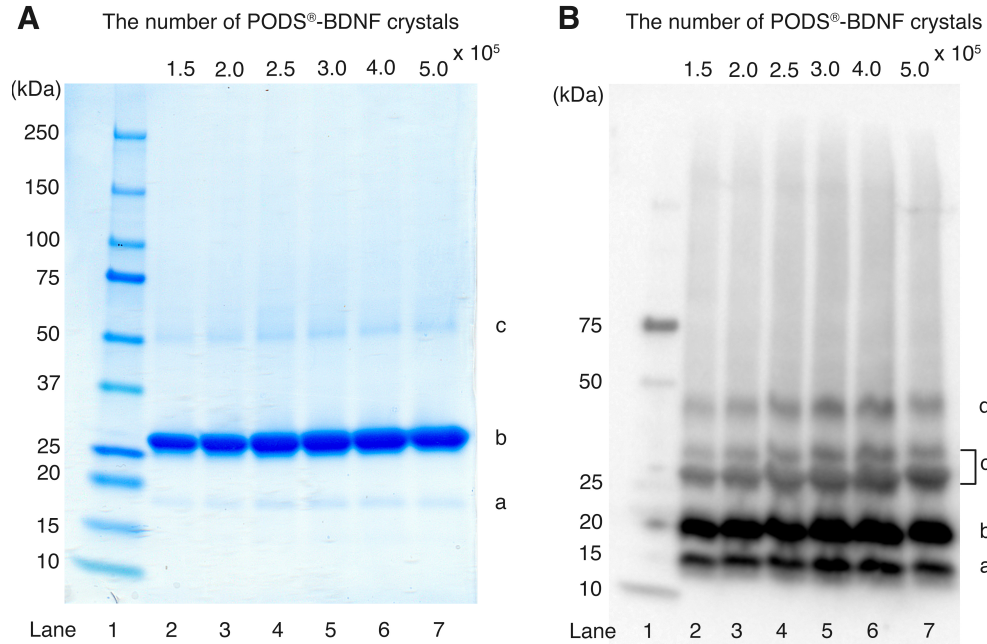


Figure 5: (A): SDS-PAGE analysis of PODS[®]-rhBDNF. Samples containing six quantities of PODS[®]-rhBDNF crystals were run on precast 4-15% polyacrylamide mini-gels and stained with Coomassie G-250 solution for visualization. Protein bands appear at approximately 18.8 (a), 28.0 (b), and 46.8 kDa (c). Lane 1: molecular weight marker. Lanes 2-7: samples containing

320 appeared to fit the nonlinear curve of Equation 2, which describes the concen-
321 tration of the intermediate product of two consecutive first-order reactions:

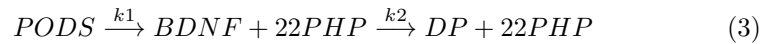
$$C_{rhBDNF} = C_{PODS} \cdot k_1 \cdot \left(\frac{e^{-k_1 \cdot t}}{k_2 - k_1} + \frac{e^{-k_2 \cdot t}}{k_1 - k_2} \right) \quad (2)$$

322 where C_{rhBDNF} is the concentration of the intermediate product rhBDNF and
323 C_{PODS} is the initial concentration of PODS[®] [43].

324 We successfully fit the data empirically to this nonlinear curve ($R^2 = 0.7891$),
325 approximating k_1 to be 0.00686 ($\frac{1}{hour}$) (See further detail in Supplementary
326 Figure S7).

327 SDS-PAGE was used to separate PODS[®]-rhBDNF crystals into its con-
328 stituent proteins to determine the molar ratio of polyhedrin to rhBDNF. Vi-

329 sualization with Coomassie G-250 solution (Figure 6A) revealed three distinct
 330 protein bands at 18.8 (a), 28.0 (b), and 46.8 (c) kDa, which correspond to the
 331 molecular weights of H1-tagged BDNF monomer, polyhedrin, and H1-tagged
 332 BDNF monomer conjoined with polyhedrin, respectively. Western blot analy-
 333 sis was subsequently conducted to confirm the identity of the 18.8 kDa band
 334 as rhBDNF. Enhanced chemiluminescence (Figure 6B) revealed four protein
 335 bands at 14.0 (a), 18.8 (b), 37.6 (c), and 46.8 (d) kDa, which correspond
 336 with the molecular weights of rhBDNF monomer, H1-tagged BDNF monomer,
 337 H1-tagged BDNF dimer, and H1-tagged BDNF monomer conjoined with poly-
 338 hedrin. Immunoblot detection of the 18.8 kDa band further validates its identity
 339 as rhBDNF. SDS-PAGE images were converted to 8-bit grayscale and mean cor-
 340 rected integrated pixel intensity values were calculated for protein bands located
 341 at 28.0 and 18.8 kDa; the protein band detected at 46.8 kDa was omitted from
 342 the final analysis. Results indicated that the molecular ratio of polyhedrin to
 343 rhBDNF is approximately 22:1 in PODS®-rhBDNF. This transforms Equation
 344 (1) into:



345 With the calculated molar ratio and rate constants for the complete molecu-
 346 lar reaction, the resulting chemical gradient with respect to time after PODS®-
 347 rhBDNF placement can be solved for any geometry by applying Fick's second
 348 Law of diffusion (Equation 4) and the appropriate boundary (Equations 5 and
 349 6) and initial conditions (Equation 7):

$$\frac{dC}{dt} = \nabla \cdot (D \cdot \nabla C) - k_2 \cdot C \quad (4)$$

350 Boundary Conditions:

$$\delta C \Big|_{walls} = 0 \quad (5)$$

351 and

$$C_{BDNF_P,i} = C_i \quad (6)$$

Initial conditions:

$$C|_{t=0} = 0 \quad (7)$$

where C is the concentration of rhBDNF, D is diffusivity of rhBDNF ($6.76 \frac{mm^2}{day}$ [44]), and $-k_2 \cdot C$ is the sink term corresponding to the degradation and cell-utilization of the rhBDNF. The first boundary condition (Equation 5) declares that the concentration of rhBDNF at the walls of the microfluidic device are fixed at 0. The second boundary condition (Equation 6) is a "continuous concentration" boundary condition denoting that the concentration of rhBDNF just behind the boundary of the PODS-rhBDNF volume ($C_{BDNF_P,i}$) is equal to the concentration of rhBDNF just beyond the same boundary in the surrounding media (C_i).

We empirically tested the FEA with two of the available Xona™ devices with differing microchannel lengths—(i.e., Xona™ -XC150 [$150 \mu m$] and Xona™ -XC450 [$450 \mu m$]). This was done first because mass (i.e., BDNF) transport from the neurotrophin compartment through the micro-groove channels into the somal compartment is an important factor in generating the concentration gradient *via* diffusion mixing. We determined that the Xona™ Microfluidics XC450 was more appropriate for this study as anatomical measurements using an emission electron microscope have demonstrated that the distance from the medial wall of the scala tympani to the SGN cell body is approximately $400 \mu m$ [?]. Furthermore, the micro-groove channels in the Xona device simulate the pores of the osseous spiral lamina and modiolus, which constitutes the separation between the scala tympani and extant SGNs [41, 42]. Please see Supplementary Figure S6 for detailed measurements of the three-dimensional mesh of the XC450 generated for the FEA.

The finite element analysis was then empirically optimized to generate an rhBDNF concentration gradient adequate for hPSC-derived ONP differentiation toward SGNs and their directed neurite extension by using various PODS®-

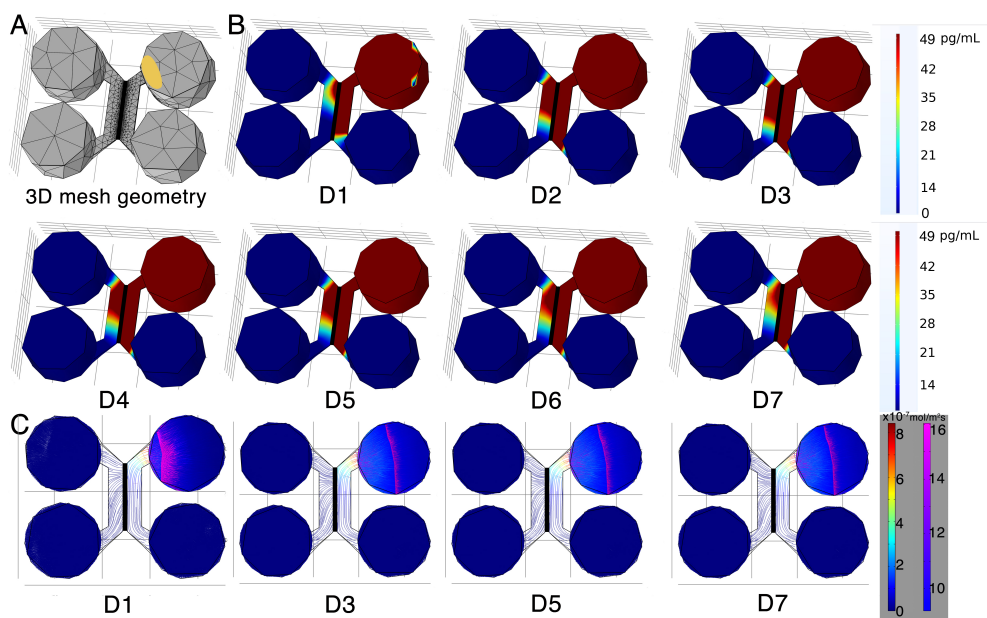


Figure 6: (A): 3D mesh geometry of a Xona™ XC450 created with Autodesk Inventor. A PODS®-rhBDNF ellipsoid disc is shown in yellow. (B): rhBDNF concentration gradient for 20,000 PODS®-rhBDNF from D1–D7. Note that the model does not account for media changes during the culture period. The corresponding color map shown has a range from 0 ng/mL to 49 pg/mL. (C): Diffusion flux ($\text{mol}/\text{m}^2\text{s}$) was computed using COMSOL Chemical Engineering module on D1, D3, D5, and D7.

378 rhBDNF quantities and time intervals. Figure 6 shows FEA-computed rhBDNF
379 concentration profiles for 20,000 PODS®-rhBDNF crystals from D1–7. Note
380 that the rhBDNF concentrations were tuned to be greater throughout D2–5
381 to promote the neuronal differentiation and neurite outgrowth observed on D7
382 (Figure 6B). Computed diffusion flux was uniform throughout D1–7 (Figure
383 6C). Also note that highest concentration of rhBDNF released from PODS®
384 crystals was greater than 50 pg/mL, the concentration sufficient for otic neu-
385 ronal differentiation and neurite outgrowth of hPSC-derived ONP 3D spheroids
386 determined with our previously published data [9]. Please see detailed discussion
387 of the empirical optimization in Supplementary Figure S8.

388 After the biological experiments, we performed quantitative analysis of PAX8
389 and GATA3 double-positive cells using immunocytochemistry to objectively
390 compare the degree of otic neuronal differentiation in the hPSC-derived ONPs.
391 PAX8 and GATA3 were selected for this analysis in accordance with our previous
392 studies indicating high expression of these protein markers in hPSC-derived late-
393 stage ONPs and early-stage hPSC-derived SGNs [8, 9, 24]. Cells were stained in
394 the somal compartment of the Xona™ device, highlighted in green in Figure 7A.
395 Figure 7B shows the resulting image of cells in the somal compartment, while
396 a heat-map representation of the percentage of double-positive cells is shown
397 in Figure 7C. It should be noted that the heat-map is sensitive to the differ-
398 ences in cell density across the channels. This was accounted for by averaging
399 the double-positivity across three biological replicates. The heat-map indicates
400 higher double-positivity in the upper region of the somal compartment, which
401 is closest to the PODS®-rhBDNF disc placement (shown as an orange ellipse
402 in Figure 7A) in the neurotrophin compartment. Double-positivity decreases as
403 distance from the PODS®-rhBDNF disc increases, supporting the presence and
404 effects of a rhBDNF neurotrophin gradient as predicted by our computational
405 model (Figure 7D).

406 We defined two hypothetical directional angles to predict the orientation of
407 hPSC-derived ONPs and neurite growth (Figure 8). The n -dimensional Eu-
408 clidean space, denoted by \mathbb{R}^n , is a linear vector space in that we can use polar

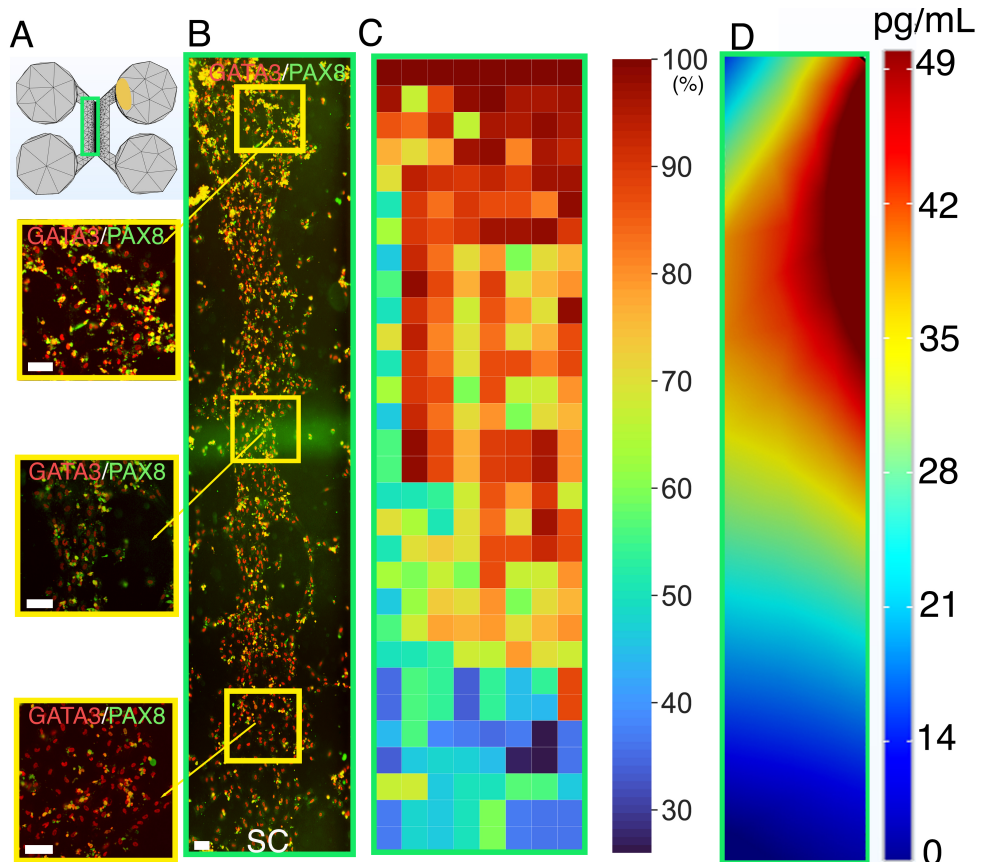


Figure 7: Human PSC-derived late-stage ONPs grown in a microfluidic device at Day 7 were stained for GATA3 (red) and PAX8 (green). (A): Mesh geometry of the microfluidic device Xona™ XC450 constructed with Autodesk Inventor. The green square indicates the cell seeding location in the somal compartment of the device. An ellipsoid PODS®-rhBDNF disc is shown in yellow. (B): Cells were analyzed by staining with neuronal markers GATA3 (red) and PAX8 (green). Yellow highlighted regions are magnified on the left. SC: somal compartment. (C): Heat-map representation of double-positivity of hPSC-derived ONPs in the device for GATA3 and PAX8 ($n = 3$). Double-positivity increases from the lower to the upper portion of the somal compartment, suggesting that the higher BDNF concentration in the upper portion of the device improves differentiation. Scale bar: 100 μ m. (D): Prediction of BDNF concentration gradient released from PODS®-rhBDNF at seven days in culture using the finite element model. The corresponding color map is shown with a range from 0–49 pg/mL.

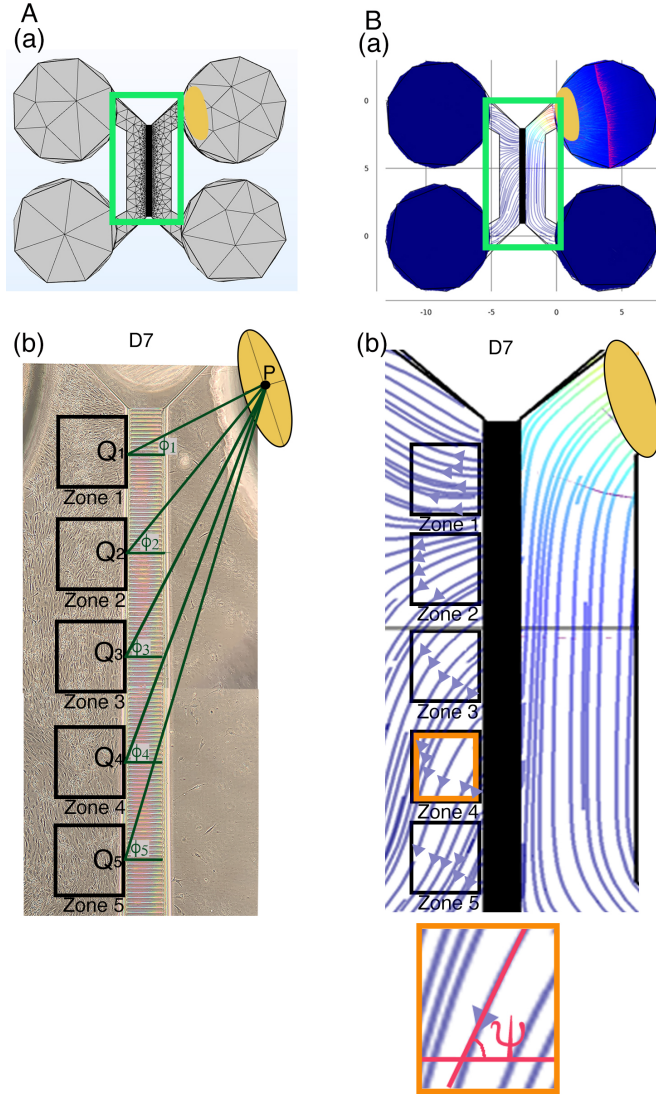


Figure 8: (A): Defining the Euclidean distance angle (EDA). (a) X-Y plane mesh geometry of a Xona™ XC450 device. Green square shows the area corresponding to the phase-contrast image below. An ellipsoid PODS®-rhBDNF disc is shown in yellow. (b) Yellow ellipse indicates the location of a disc containing PODS®-rhBDNF crystals (P: the center of this ellipse). In the somal compartment of the Xona™ XC450 device, we defined Zone 1–5, shown in black squares. A line was drawn from the center of the PODS®-rhBDNF disc (P) to (Q_{1-5}) (i.e., the side nearest to microgroove channels) of a pre-designated square (shown as a black square, zone 1–5) [i.e.,zone 1–5]. The Euclidean distance angle (EDA) for zone 1–5 was defined as ϕ_i , $i = 1-5$. (B): Defining diffusion flux angle (DFA). (a) Diffusion flux in the Xona™ XC450. Green squared area shows somal and neurotrophin compartments, which are magnified in (b). (b) Magnified image of diffusion flux in Zones 1–5 in the Xona™ XC450. Orange highlighted zone (zone 4) was magnified at the bottom of (b), defining the DFA (ψ).

409 coordinates to compute the directionality of cells and neurites [45]. Here, we
410 used $n = 1$ and 2. For one-dimensional Euclidean space ($n = 1$), we simply drew
411 a line for the Euclidean distance—the shortest distance between two points as
412 shown in Figure 8A(b) (dark green lines). The two points were 1) the center
413 point of the PODS®-rhBDNF disc (P) and 2) the mid point of the medial side
414 (i.e., the near side to microgroove channels) of a pre-designated square
415 (shown as a black square, zones 1–5 in Figure 8), respectively. The Euclidean
416 distance angle (EDA), ϕ_i , was defined as the angle between the horizontal line
417 zero direction and the line PQ_i that consists of the Euclidean distance where i
418 = 1–5.

419
420 For two-dimensional Euclidean space ($n = 2$), we utilized Fick’s first law,
421 which dictates that the diffusion flux (D) is proportional to the concentration
422 gradient (C) [46]:

$$\mathbf{J} = -D\nabla C \quad (8)$$

423 Based on this theorem, the direction of a flow vector can be used to represent
424 the concentration gradient for directionality. We hypothesized that cell orien-
425 tation is directionally controlled by the flux vector (driven by the concentra-
426 tion gradient). Figure 8B shows the flow vectors in the somal compartment at Day 7
427 computed by the COMSOL Chemical Reaction Engineering module. We aver-
428 aged the 10 flow vectors in each of five zones in Figure 8 to compute the diffusion
429 flux angle (DFA), ψ_i , where $i = 1–5$ in Figure 8. To lighten the computational
430 intensity, we reduced the dimension from 3D to 2D to compute diffusion flux.
431 Please see justification in Supplementary Data. All of the computed EDAs and
432 DFAs can be found in Supplementary Table 2.

433 Figure 9 shows time-series of microscopic phase-contrast photomicrographs
434 obtained on days 1, 3, and 7 in the five zones in the Xona™ XC450. Each
435 preferred orientation of any given cell was computed and then plotted on a
436 polar diagram (blue circle). Mean vector angle (MVA, shown as a red line on

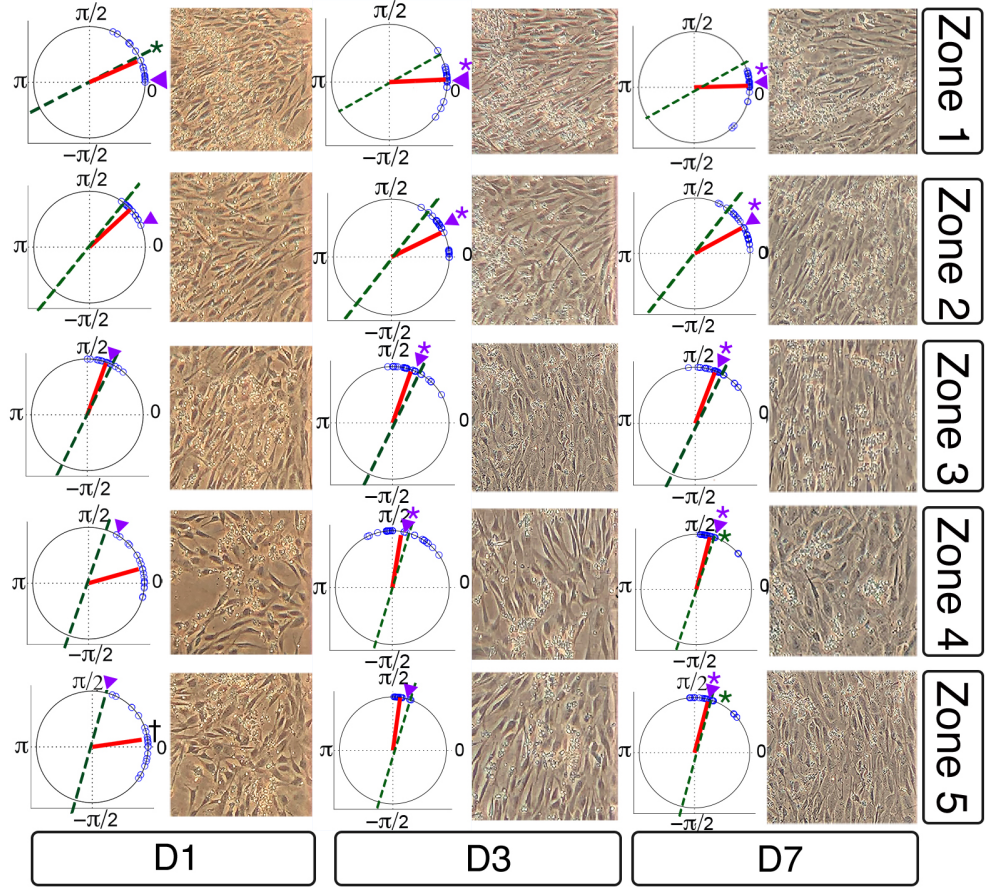


Figure 9: Preferred cell orientation analysis. Sequential phase-contrast images of the somal compartment of the Xona™ XC450 device in zones 1–5 (see Figure 8) on day 1 (D1), day 3 (D3), and day 7 (D7). A corresponding polar histogram indicates preferred orientation of hPSC-derived ONPs as an angle (0– 2π radians) in blue circles. Mean vector angle is shown in red line. Green dotted line shows Euclidean Distance Angle (EDA) and purple triangle indicates Diffusion Flow Angle (DFA). † symbol indicates that p value > 0.01 . * symbol indicates that the mean vector angle fits within the 95% confidence internal ($\alpha < 0.05$).

437 Figure 9) and median vector angle were computed. All of the polar diagrams
438 in Figure 9 show that preferred orientation of hPSC-derived ONPs distribute in
439 an unimodal distribution. We also confirmed that a von Mises distribution is
440 appropriate for these sets of data (See Supplementary Figure S9). We performed
441 further analysis to assess if the cells had a tendency to be oriented in a certain
442 direction. We used the Rayleigh test of uniformity to evaluate whether there
443 was statistical evidence of circular directionality [32]. Computed *p* values for all
444 the 15 conditions were less than 0.05, demonstrating that all of the conditions
445 had statistically significant directionality. Furthermore, to discern whether the
446 observed angles had a tendency to cluster around the two hypothetical angles
447 (i.e., EDA and DFA), we then performed the V test. Likewise, *p* values for
448 all 15 samples were less than 0.05 except one (Zone 5 on Day 1), underscoring
449 that most of the conditions had statistically significant tendencies to cluster
450 around the EDAs and DFAs. Additionally, we performed one sample test for
451 the mean vector angle, similar to a one sample t-test on a linear scale. There
452 was only one condition (Zone 1, day 1) that was statistically significant for EDA
453 clustering, whereas most of the conditions on Day 3 and 7 were statistically
454 significant for DFA clustering. Therefore, our results demonstrate that hPSC-
455 derived ONPs had greater tendency to cluster around DFAs than EDAs. All
456 computed statistical values are shown in Supplementary Table S2.

457 To evaluate the direction of neurites of hPSC-derived ONPs, we first de-
458 fined EDA in Region 1-3 (ϕ'_j , $j = 1 - 3$) (Figure 10A) and DFA (ψ'_j , $j = 1-3$);
459 similarly defined ϕ_i and ψ_i as in Figure 8. All of the EDAs and DFAs defined
460 here can be found in Supplementary Table S3. Polar histograms of the neurite
461 direction angle in Regions 1–3 indicate that the two longest neurites were bi-
462 modal in nature (Figure 10B). In contrast, polar histograms of those cultured
463 with rhBDNF (negative control) and 800,000 PODS[®]-BNDF (positive control)
464 did not indicate bimodal distribution—the neurites did not show directionality
465 (Figure 10C). The Rayleigh test of uniformity for both the positive and neg-
466 ative control were greater than 0.05, underscoring that both of the conditions
467 had no statistically significant directionality (Supplementary Table S3: high-

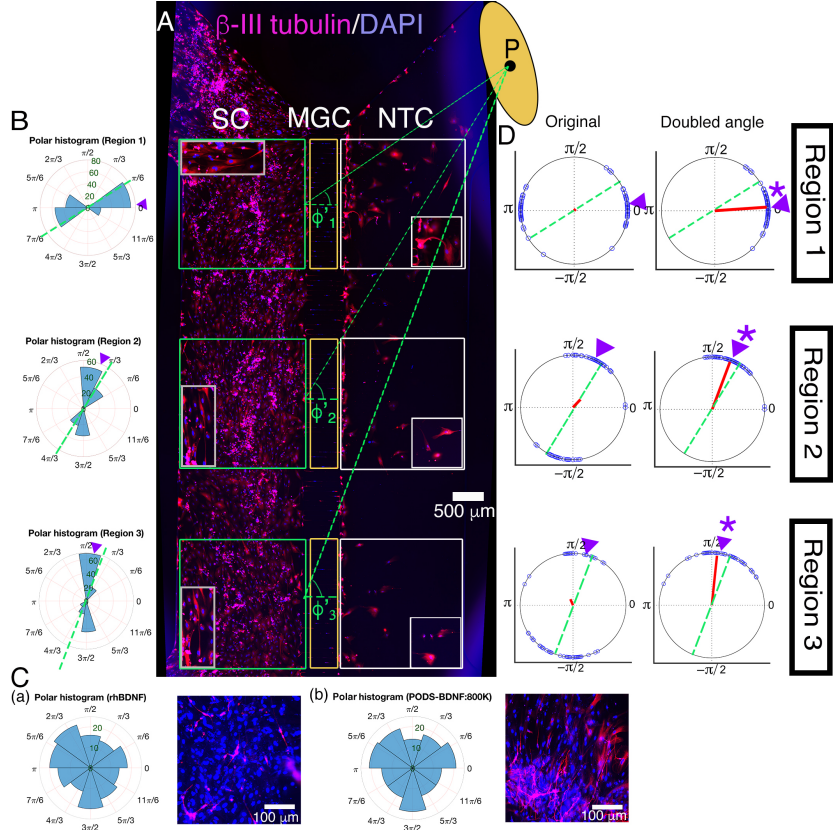


Figure 10: (A): Immunohistochemistry of hPSC-derived ONPs cultured in the Xona™ XC450 for seven days with β -III-Tubulin (pink fluorescence) and DAPI (blue fluorescence). A green line was drawn from the center of the BDNF disc (P) to the mid point of each of three pre-determined squares (Regions 1–3) in the somal compartment to define Euclidean Distance Angle (EDA: ϕ_i^i , $i = 1 - 3$). Green square: somal compartment (SC); yellow square: microgroove channels (MGC); white square: Neurotrophin compartment (NTC). High-power magnified images of the NTC and SC are shown. An ellipsoid PODS®-rhBDNF disc is shown in yellow. P: the center of the disc. (B): Polar histogram of neurite directional angles of hPSC-derived ONPs in the Xona™ XC450 at Day 7 (D7). The two longest neurites were measured. EDA: green dotted line. DFA: purple triangle. (C): (a) Right: Polar histogram of neurite directional angles of hPSC-derived ONPs cultured with 20 ng/mL of recombinant human BDNF for seven days. Left: Corresponding photomicrograph of immunocytochemistry with β -III tubulin (pink) and DAPI (blue). (b) Right: Polar histogram of neurite directional angles of hPSC-derived ONPs cultured with 800,000 of PODS®-rhBDNF for seven days. Left: Corresponding photomicrograph of immunocytochemistry with β -III tubulin (pink) and DAPI (blue). (D): A circular plot of neurite directional angle of hPSC-derived ONPs in Region 1–3. Once again, the two longest neurites were plotted on a unit circle. Right column: Original directional angle distribution. Left column: the method of doubling the angle applied to the original data. Each datum point is shown as a blue circle. Mean vector angle is shown as a red line. Green dotted line shows Euclidean Distance Angle (EDA) and purple triangle indicates Diffusion Flow Angle (DFA). * symbol indicates that the mean vector angle fits within the 95% confidence internal ($\alpha < 0.05$.)

468 lighted in green). We also analyzed the direction of the neurites using circular
469 statistics. To obtain more realistic mean vector angles, we doubled each angle
470 and reduced the multiples modulo by 360°. In circular statistics, the bimodal
471 distributed data can be transformed into a unimodal data by doubling the angle
472 [32]. The mean vector angles in Figure 10D (right column) suggest the circum-
473 stance in which the vectors were canceled out between the two groups of angles
474 distributed in a bimodal fashion, resulting in inaccurate representation. A cir-
475 cular plot in Figure 10D (right column) showed doubled angles, representing
476 actual representation of the neurite vector angles. In all of the three regions,
477 the Rayleigh test and V test for EDA and DFA indicate directionality (Sup-
478 plementary Table S3). One sample test for the mean vector angles in Region
479 1–3 indicated that they were not statistically different from DFA, but all of the
480 three mean vector angles were statistically different from EDA.

481 Devices were stained for β -III tubulin to track neurite growth and extension
482 across the micro-groove channels in addition to cell migration in three selected
483 regions (Figure 10A). The location of the PODS®-rhBDNF disc in relation to
484 the regions of interest in Figure 11A is indicated by a yellow circle. Quantitative
485 analyses were performed and summarized in Figure 11B. Our data indicate that
486 neurite length is dependent on rhBDNF concentration, with greater amounts
487 of PODS®-rhBDNF promoting longer neurite growth (Figure 11B(a)). Lesser
488 amounts of PODS®-rhBDNF, however, are necessary to create an appropriate
489 concentration gradient. In the presence of 20,000 PODS®-rhBDNF, both neu-
490 rite extension into the microchannels and cell migration into the neurotrophin
491 compartment are greatest in the region closest to the rhBDNF source and de-
492 crease further from the PODS®-rhBDNF (Figure 11B(b,c)). Cell migration
493 is dependent on the distance from the source of rhBDNF, thus suggesting the
494 presence of a rhBDNF gradient as predicted by our model.

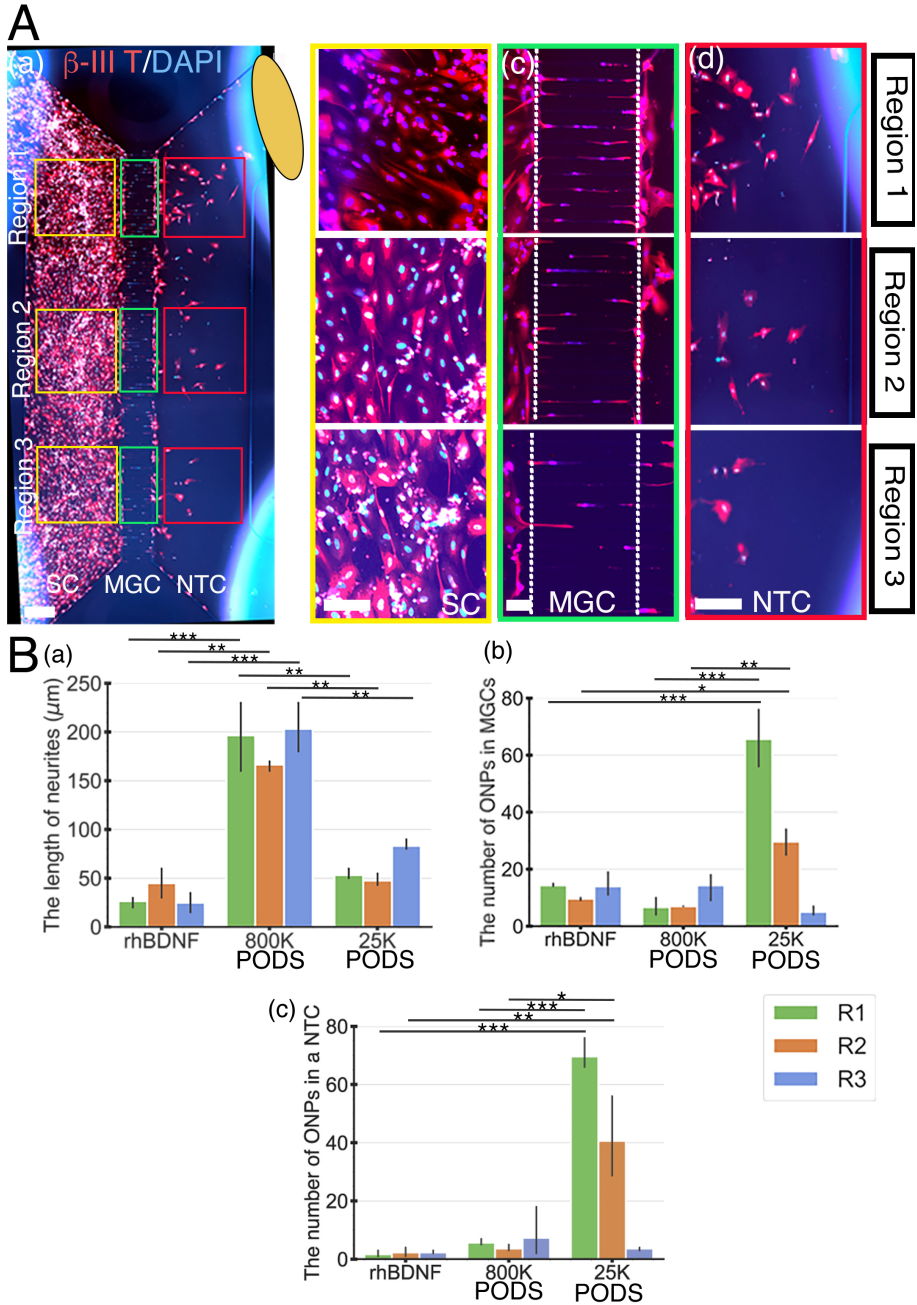


Figure 11: Human PSC-derived late-stage ONPs in the microfluidic device were stained with β -III tubulin (red) and DAPI (blue) to measure cell migration. (A): Late-stage ONPs stained after seven days in culture (a) with regions highlighted and magnified in the somal compartment (b), microgroove channels (c), and neurotrophin compartment (d). SC: somal compartment, MGC: microgroove channels, NTC: neurotrophic compartment. An ellipse-shaped PODS®-rhBDNF disc is shown in yellow. Scale bar (a): 500 μm ; (b)–(d): 100 μm . (B): Quantitative analyses of cell migration and neurite extension in devices using recombinant human BDNF, 800,000 PODS®-rhBDNF, or 20,000 PODS®-rhBDNF. * : $p < 0.05$, **: $p < 0.01$, ***: $p < 0.001$.

495 **4. Discussion**

496 *4.1. Challenges of neurotrophin treatment in the inner ear*

497 This proof-of-concept study for the realization of a neuroregenerative nexus
498 was conducted to ascertain its scientific/technological parameters in a controlled
499 *in vitro* environment. Neurotrophin gradients have been studied in multiple
500 contexts [47, 48, 49]. However, it has not been feasible to reliably provide, and
501 maintain, such a gradient to neurons *in vivo*, primarily because of technical
502 challenges including failure to provide a reliably sustainable source in addition
503 to practical surgical implantation. Furthermore, while neurotrophin treatment
504 has been recognized as a potential treatment for sensorineural hearing loss, there
505 has not been long-term clinical success in this avenue to date. Most recent rele-
506 vant clinical trials used adeno-associated virus (AAV2) to deliver BDNF to the
507 brain [50]. Although compelling, this treatment does not attempt to precisely
508 control the concentration of BDNF, which could potentially interfere with nor-
509 mal functions in the target organ [51]. Furthermore, this treatment may not be
510 applicable to the inner ear, as MR-guided procedure is technically infeasible in
511 the setting of the inner ear. In this study, we used PODS®-rhBDNF to generate
512 and maintain a neurotrophic gradient in a controlled manner. Our results indi-
513 cate that 20,000 PODS-rhBDNF crystals allowed for a rhBDNF neurotrophin
514 gradient such that hPSC-derived ONPs survived, differentiated toward human
515 SGNs, and established directional neurite outgrowth in a microfluidic device.
516 Furthermore, our proposed solution has greater potential to be translated into
517 clinical practice; in addition to its proven natural self-sustainability, we have
518 previously demonstrated that implantation of PODS-rhBDNF is met with little
519 immune rejection when embedded in a nanofibrillar cellulose hydrogel in mice
520 [9].

521 *4.2. Microfluidic device-generated gradient*

522 We utilized a microfluidic device to advance our understanding of direc-
523 tional neurite growth and otic neuronal differentiation in response to a rhBDNF

concentration gradient [52]. Among many *in vitro* concentration gradient sustaining culture devices, microfluidic devices have overcome many of the deficits that conventional platforms (i.e., the Boyden chamber, Dunn chambers, or compartmentalized diffusion chambers) face [52]. Conventional platforms tend to be sub-optimal in manipulating small volumes of fluid at the order of microliters. Growth factors and proteins can be used in small quantities in our microfluidic device, and cultured stem cells are able to interact with endogenous factors at biologically relevant concentrations. As mentioned earlier, this microenvironment more accurately represents *in vivo* conditions. The Xona™ device can be used to create and sustain a three-dimensional concentration gradient over time (duration and diffusion profile dependent on the chemical kinetics of the molecule) because of its microchannel array. The device limits convective flow in the gradient-forming areas by introducing microgroove channels that generate high fluidic resistance, thereby limiting flow to diffusion. The high resistance of the microchannel array also prolongs diffusion across them, thereby increasing gradient formation and decreasing gradient steepness (essentially elongating it). These features motivated us to generate an FEM to predict the rhBDNF gradients resulting from different numbers of PODS®-rhBDNF crystals. Note, however, that this environment is geometrically different from the micro-environment in the inner ear—a mesh geometry of the cochlea will be needed to compute the PODS®-rhBDNF crystal number for implementation in animals, as well as in further clinical translation.

4.3. Brain-derived neurotrophic factor

Over the course of the past 20–30 years, it has been established that BDNF mediates survival and differentiation activities of SGNs by binding and activating tyrosine kinase receptor kinase B (TrkB), a member of the larger family of Trk receptors [20]. Numerous studies have reported that BDNF can palliate SGN degeneration in ototoxically deafened animals, a widely accepted model for retrograde trans-synaptic SGN degeneration secondary to hair cell destruction [13, 14, 53, 54]. Additionally, it has been confirmed that there is a positive

554 correlation between SGN counts and CI performance [55]. It is then safe to
555 presume that BDNF application in CI recipients would enhance overall CI per-
556 formance, by preserving extant SGNs and their neurites. Although promising,
557 BDNF treatment in humans has not been implemented in the inner ear as simply
558 introducing BDNF into the inner ear poses significant hurdles.

559 Unsuccessful BDNF treatment is attributed to several factors [56]. The
560 blood half-life of BDNF protein is extremely short, lasting only 1–10 minutes
561 in plasma [57, 58] and one hour in CSF [59]. Due to BDNF’s high degrada-
562 tion rate, simple introduction of BDNF in solution would require continuous
563 replenishment, which is impractical in the clinical setting. Furthermore, simply
564 introducing BDNF in solution would promote non-directional neurite growth
565 where directed neurite growth is essential, especially in the case of our proposed
566 bioactive CI, due to the lack of a concentration gradient to guide the growth. Di-
567 recting neurite growth towards the CI electrode array is pivotal in the ultimate
568 goal of enhancing performance through the narrowing of the electrode-neuron
569 gap. The PODS® system provides a gradual release of growth factor from a
570 localized origin. This steady supply of BDNF from a localized origin not only
571 generates a concentration gradient, but maintains it over time. As shown in
572 Figure 6, it is unmistakable that the slow-release nature of PODS®-rhBDNF
573 results in a concentration gradient over the course of Day 1–7. As shown in
574 Figures 7–11, careful calibration of the resulting BDNF gradient can lead to
575 the promotion of hPSC-derived ONP differentiation towards SGN lineage and
576 directed neurite extension.

577 It should be noted that our FEM assumes free diffusion of the rhBDNF
578 protein. In biological cell-culture conditions, rhBDNF released from PODS®-
579 rhBDNF has tendency to adhere to walls of the culture device, due to its nature
580 as a "sticky" protein of about 27 kDa (mature BDNF dimer) that is positively
581 charged under physiological conditions (isoelectric point, pI = 9.4) [60]. As such,
582 the physio-chemical properties of rhBDNF have rendered the protein prone to
583 diminished diffusive transport. This phenomenon was observed in preliminary
584 data where the ONPs failed to survive past 1–3 days of culture (data not shown).

585 To circumvent this issue we infused the culture media with a carrier protein (i.e.,
586 BSA), hypothesizing that the albumin would act as a carrier for the released
587 rhBDNF and allow for free diffusive transport throughout the microfluidic de-
588 vice [61]. This hypothesis is supported by our sets of biological validation data
589 (Figures 7–11) clearly showing that hPSC-derived ONPs responded positively
590 to the modification; they exhibited the expected cell characteristics, body orien-
591 tation, unidirectional neurite extension, and neurite length. Note that albumin
592 is the single most highly concentrated protein in the perilymph [62], therefore,
593 an artificially introduced carrier protein would not be required in future *in vivo*
594 studies.

595 *4.4. Intracellular signaling initiated by the Tyrosine kinase B receptor*

596 Another issue for consideration in the interpretation of our results is the
597 intracellular cell-signaling mechanism elicited by rhBDNF. Human BDNF (ma-
598 ture dimeric form) binds with high affinity to the TrkB receptor. The binding
599 of BDNF to a TrkB receptor is integral to the pro-neuronal effects of BDNF
600 [20]. Upon binding, TrkB dimerizes and activates intrinsic kinase activities and
601 other complex sets of intracellular signaling cascades, beyond the scope of this
602 study. It should be noted that activation also initiates internalization by en-
603 docytosis and subsequently transports the protein to the soma [63]. Therefore,
604 the pro-neuronal effects of rhBDNF in our results may be highly dependent on
605 the status of the TrkB receptors of the cell membranes of hPSC-derived ONPs.
606 Our previous study has demonstrated strong expression of the TrkB receptors
607 on derived ONPs [24], however, more detailed studies on TrkB receptors of
608 hPSC-derived ONPs and SGNs are needed to deepen understanding.

609 *4.5. Degradation of PODS® crystals by protease activity*

610 In cell culture, degradation of PODS®-rhBDNF is likely due to the enzy-
611 matic activity of cell-secreted proteases. The proteases break down the peptide
612 bonds of the encasing polyhedrin protein, creating openings in the structure to

allow release of the rhBDNF. Therefore, the presence of proteases is imperative for the proper implementation of PODS® technology. These proteases are additionally responsible for subsequent degradation of the released rhBDNF. Because cells were not present in the culture media used for the PODS® degradation kinetics experiments, we infused the media with 10% FBS, which inherently contains proteases. Furthermore, since the cells and PODS are initially segregated into separate compartments within the culture device, cell-secreted proteases are unlikely to reach and degrade the PODS in time to support ONP survival and differentiation, which was apparent in experiments conducted without the addition of FBS (data not shown). Infusion with FBS was therefore required in these experiments as well. For clinical translation, however, we presume that cell-secreted proteases will be readily present in the inner ear and therefore preclude the need for artificial supplementation.

4.6. A concept design: neuroregenerative nexus

The plateau in CI performance in treatment of sensorineural hearing loss has driven researchers to develop innovative supplementary treatment strategies to push the field past this hurdle. Our approach strives to directly address the issue at its core: the electrode-neuron gap—which can lead to serious implications including low spatial frequency resolution and high power consumption. The data presented here can be used as a launchpad for the neuroregenerative nexus (NRN). The proposed NRN is a biointerface concept that integrates a long-term release source of neurotrophins (i.e., BDNF) with a bioengineered scaffold to facilitate and maintain a neurotrophic factor gradient. Embedding the source (e.g., PODS®-rhBDNF) in a biocompatible matrix ensures localization as well as a mechanism to fine-tune degradation and release kinetics. Implanted in conjunction with the CI, the NRN acts as a supportive bridge between extant SGNs and transplanted hPSC-derived late-stage ONPs, which are localized on the implant electrodes themselves (see Figure 1 for schematic). The NRN would promote survival of both cell populations, differentiation of the hPSC-derived late-stage ONP transplants towards SGNs, directional neu-

rite growth, and synaptogenesis between the two cell populations, effectively creating a neuronal network between the patient and the CI. As a result, each electrode would stimulate cell bodies at exceptionally high resolution, essential for greater tonal differentiability (required for effective social interaction and music appreciation) and furthermore, increased quality of life for millions. The successful outcomes presented in this article are pivotal for the realization of a neuroregenerative nexus that is effective in the *in vivo* environment.

4.7. *The limitations of this study and future direction*

The reduction of the spacial dimension to 2D for flux analysis certainly affected the flux vector, which determines the predicted concentration vector. Given that the thickness (i.e., Z-axis) of the microfluidic device was 100 μm , we estimated that the effect was minimal. In the future, we plan to use hPSC-derived 3D spheroids in the somal compartment so that flux vector and concentration gradient vector can more accurately model cell behavior. In this way, we will be able to circumvent the need to reduce diffusion calculations to 2D for computation performance in the modeling.

We generated an FEM that modeled rhBDNF's biological transport phenomenon from a PODS[®]-rhBDNF disc throughout the Xona™ device. Note that in this model, we focused on the major dependent variable, the concentration and diffusion profile of rhBDNF, to model the biological phenomenon. Other physical variables that promote cell migration, otic neuronal differentiation, and neurite growth were not taken into consideration. These variables include electrotaxis (electrical potential), durotaxis (matrix stiffness [i.e., laminin 511 in our case]) [64], mechanotaxis (cell strain), and lastly cell migration by random walk [65]. In future studies, we will take these variables into consideration to more accurately represent the migration and neurite growth of hPSC-derived ONPs.

Insufficient contrast between cells and background in phase contrast images led to inaccuracies in cell orientation computation for some images. To address this issue, poor quality images were disregarded in the quantitative analysis.

673 We occasionally used manual measurement for accuracy. Our future study may
674 entail automated time-series cell analysis, which would allow more accurate
675 measurement. Another alternative to address this issue would be with cell
676 membrane staining in the future.

677 While 20,000 PODS®-rhBDNF crystals were necessary for otic neuronal
678 differentiation and directional neurite outgrowth of hPSC-derived ONPs, this
679 condition may not be sufficient. For instance, it is still not understood whether
680 the effects of other neurotrophic factors such as Neurotrophin-3 (NT-3) and
681 Glial cell line-derived neurotrophic factor could have a positive effect on ONP
682 growth [20, 66, 67]. We plan to investigate the effects of these and other neu-
683 rotrophic factors in future studies. Other aspects that could impact directional
684 neurite growth include endogenous factors secreted from hPSC-derived ONPs.
685 While our previous study demonstrated that hPSC-derived ONPs only secreted
686 negligible amounts of BDNF, quantified by ELISA [9], we currently lack data
687 on other neurotrophins and molecules that can affect directional neurite growth
688 in the inner ear. Additionally, previous studies indicate that neurotrophic sup-
689 port of SGNs is mainly composed of BDNF and neurotrophin-3 (NT-3) [20, 60].
690 Therefore, the potential confounding effects of other neurotrophic factors (i.e,
691 NT-3) and molecules secreted from hPSC-derived SGNs require further investi-
692 gation.

693 Despite these limitations, the presented evidence is clear and well grounded
694 –a precisely controlled and maintained BDNF concentration gradient is neces-
695 sary for directional neurite extension.

696 **Conclusions**

697 We successfully promoted survival, neuronal differentiation toward SGNs,
698 and directed neurite extension of hPSC-derived ONPs by generating a neu-
699 rotrophin gradient. This technique can allow for controlled neurite growth in
700 transplanted hPSC-derived ONPs, as well as native, extant SGNs in the inner
701 ear. This proof-of-concept study translates to a step toward next-generation

702 bioactive CI technology.

703 **Acknowledgment**

704 This work was supported by the American Otological Society Clinician Sci-
705 entist Award (AJM), the Triological Society/American College of Surgeons
706 Clinician Scientist Award (AJM), the Department of Otolaryngology of North-
707 western University (AJM), the NIH (NIDCD) K08 Clinician Scientist Award
708 K08DC13829-02 (AJM), and the Office of the Assistant Secretary of Defense of
709 Health Affairs through the Hearing Restoration Research Program (Award #:
710 RH170013:WU81XWUH-18-0712). Imaging work was performed at the North-
711 western University Center for Advanced Microscopy, which is generously sup-
712 ported by NCI CCSG P30 CA060553 awarded to the Robert H. Lurie Com-
713 prehensive Cancer Center, for which we thank Peter Duhly, Constadina Ar-
714 vanitis, Ph.D., David Kirchenbuechler, Ph.D., and Wensheng (Wilson) Liu,
715 M.D. Some of microfluidic device experiments were performed in the Analytical
716 bioNanoTechnology (ANTEC) Core Facility of the Simpson Querrey Institute
717 at Northwestern University, which is supported by the Soft and Hybrid Nan-
718 otechnology Experimental (SHyNE) Resource (NSFECCS-1542205). We thank
719 Shreyas Bharadwaj (Cornell University), Kyle Coots (Midwestern University),
720 Andrew Oleksijew (the University of Nebraska), Duncan Chadly (California In-
721 stitute of Technology), and Shun Kobayashi (the University of Texas at Austin)
722 for their contribution to the earlier phases of this project. We thank Sara Dun-
723 lop (Department of Neurology, Northwestern University), and Dr. Jacqueline
724 Bond (the University of California San Diego) for assistance in Western Blot
725 and SDS-PAGE experiments. We also thank Dr. Georgia Minakaki (Depart-
726 ment of Neurology, Northwestern University) on assistance in ELISA. Finally,
727 our thanks and appreciation go to our collaborator, Dr. Christian Pernstich
728 (Cell Guidance Systems), for continuous support and stimulating discussions
729 on this project since 2015.

730 **References**

- 731 [1] J. G. Naples, M. J. Ruckenstein, Cochlear Implant., Otolaryngologic Clinics
732 of North America 53 (1) (2020) 87–102. doi:10.1016/j.otc.2019.09.
733 004.
- 734 [2] B. S. Wilson, M. F. Dorman, Cochlear implants: A remarkable past
735 and a brilliant future, Hearing Research 242 (1-2) (2008) 3–21. arXiv:
736 NIHMS150003, doi:10.1016/j.heares.2008.06.005.
- 737 [3] C. Frick, M. Müller, U. Wank, A. Tropitzsch, B. Kramer, P. Senn, H. Rask-
738 Anderson, K. H. Wiesmüller, H. Löwenheim, Biofunctionalized peptide-
739 based hydrogels provide permissive scaffolds to attract neurite outgrowth
740 from spiral ganglion neurons, Colloids and Surfaces B: Biointerfaces 149
741 (2017) 105–114. doi:10.1016/j.colsurfb.2016.10.003.
- 742 [4] S. Hahnewald, A. Tscherter, E. Marconi, J. Streit, H. R. Widmer, C. Gar-
743 nham, H. Benav, M. Mueller, H. Löwenheim, M. Roccio, P. Senn, Response
744 profiles of murine spiral ganglion neurons on multi-electrode arrays., Journal
745 of neural engineering 13 (1) (2016) 16011. doi:10.1088/1741-2560/
746 13/1/016011.
- 747 [5] R. K. Shepherd, S. Hatsushika, G. M. Clark, Electrical stimulation of
748 the auditory nerve: The effect of electrode position on neural excitation,
749 Hearing Research 66 (1) (1993) 108–120. doi:10.1016/0378-5955(93)
750 90265–3.
- 751 [6] M. Tykocinski, L. T. Cohen, B. C. Pyman, T. Roland, C. Treaba, J. Pal-
752 amara, M. C. Dahm, R. K. Shepherd, J. Xu, R. S. Cowan, N. L. Cohen,
753 G. M. Clark, Comparison of electrode position in the human cochlea using
754 various perimodiolar electrode arrays., The American journal of otology
755 21 (2) (2000) 205–211. doi:10.1016/S0196-0709(00)80010-1.
- 756 [7] A. Roemer, U. Köhl, O. Majdani, S. Klöß, C. Falk, S. Haumann, T. Lenarz,
757 A. Kral, A. Warnecke, Biohybrid cochlear implants in human neurosensory

- 758 restoration., Stem cell research and therapy 7 (1) (2016) 148. doi:10.
759 1186/s13287-016-0408-y.
- 760 [8] R. A. Heuer, K. T. Nella, H. T. Chang, K. S. Coots, A. M. Oleksijew,
761 C. B. Roque, L. H. Silva, T. L. McGuire, K. Homma, A. J. Matsuoka,
762 Three-dimensional otic neuronal progenitor spheroids derived from human
763 embryonic stem cells, *Tissue Engineering - Part A* 27 (3-4) (2021) 256–269.
764 doi:10.1089/ten.tea.2020.0078.
- 765 [9] H.-T. Chang, R. A. Heuer, A. M. Oleksijew, K. S. Coots, C. B. Roque, K. T.
766 Nella, T. L. McGuire, A. J. Matsuoka, An Engineered Three-Dimensional
767 Stem Cell Niche in the Inner Ear by Applying a Nanofibrillar Cellulose
768 Hydrogel with a Sustained-Release Neurotrophic Factor Delivery System,
769 *Acta Biomaterialia* 108 (2020) 111–127. doi:<https://doi.org/10.1016/j.actbio.2020.03.007>.
- 770 [10] L. Taylor, L. Jones, M. H. Tuszyński, A. Blesch, Neurotrophin-3 gradients
771 established by lentiviral gene delivery promote short-distance axonal bridg-
772 ing beyond cellular grafts in the injured spinal cord, *Journal of Neuroscience*
773 26 (38) (2006) 9713–9721. doi:10.1523/JNEUROSCI.0734-06.2006.
- 774 [11] P. Senn, M. Roccio, S. Hahnewald, C. Frick, M. Kwiatkowska, M. Ishikawa,
775 P. Bako, H. Li, F. Edin, W. Liu, H. Rask-Andersen, I. Pyykkö, J. Zou,
776 M. Mannerström, H. Keppner, A. Homsy, E. Laux, M. Llera, J. P. Lel-
777 louche, S. Ostrovsky, E. Banin, A. Gedanken, N. Perkas, U. Wank, K. H.
778 Wiesmüller, P. Mistrík, H. Benav, C. Garnham, C. Jolly, F. Gander, P. Ul-
779 rich, M. Müller, H. Löwenheim, NANOCI-Nanotechnology Based Cochlear
780 Implant with Gapless Interface to Auditory Neurons, *Otology and Neuro-
781 tology* 38 (8) (2017) e224—e231. doi:10.1097/MAO.0000000000001439.
- 782 [12] G. J. Goodhill, H. Baier, Axon Guidance: Stretching Gradients to
783 the Limit, *Neural Computation* 10 (3) (1998) 521–527. doi:10.1162/
784 089976698300017638.

- 786 [13] L. N. Gillespie, G. M. Clark, P. F. Bartlett, P. L. Marzella, BDNF-induced
787 survival of auditory neurons in vivo: Cessation of treatment leads to ac-
788 celerated loss of survival effects, *Journal of Neuroscience Research* 71 (6)
789 (2003) 785–790. doi:10.1002/jnr.10542.
- 790 [14] L. N. Pettingill, R. L. Minter, R. K. Shepherd, Schwann cells geneti-
791 cally modified to express neurotrophins promote spiral ganglion neuron
792 survival in vitro, *Neuroscience* 152 (3) (2008) 821–828. doi:10.1016/j.
793 neuroscience.2007.11.057.Schwann.
- 794 [15] R. K. Shepherd, A. Coco, S. B. Epp, Neurotrophins and electrical stim-
795 ulation for protection and repair of spiral ganglion neurons following
796 sensorineural hearing loss, *Hearing Research* 242 (2009) 100–109. doi:
797 10.1016/j.heares.2007.12.005.Neurotrophins.
- 798 [16] B. Baseri, J. J. Choi, T. Deffieux, G. Samiotaki, Y. S. Tung, O. Olu-
799 molade, S. A. Small, B. Morrison, E. E. Konofagou, Activation of sig-
800 naling pathways following localized delivery of systemically administered
801 neurotrophic factors across the bloodbrain barrier using focused ultra-
802 sound and microbubbles, *Physics in Medicine and Biology* 57 (7). doi:
803 10.1088/0031-9155/57/7/N65.
- 804 [17] K. Ikeda, S. Nagaoka, S. Winkler, K. Kotani, H. Yagi, K. Nakanishi,
805 S. Miyajima, J. Kobayashi, H. Mori, Molecular Characterization of Bom-
806 byx mori Cytoplasmic Polyhedrosis Virus Genome Segment 4, *Journal of*
807 *Virology* 75 (2) (2001) 988–995. doi:10.1128/jvi.75.2.988–995.2001.
- 808 [18] T. Suzuki, T. Kanaya, H. Okazaki, K. Ogawa, A. Usami, H. Watanabe,
809 K. Kadono-Okuda, M. Yamakawa, H. Sato, H. Mori, S. Takahashi, K. Oda,
810 Efficient protein production using a Bombyx mori nuclear polyhedrosis
811 virus lacking the cysteine proteinase gene, *Journal of General Virology*
812 78 (12) (1997) 3073–3080. doi:10.1099/0022-1317-78-12-3073.
- 813 [19] H. Mori, R. Ito, H. Nakazawa, M. Sumida, F. Matsubara, Y. Minobe,
814 Expression of Bombyx mori cytoplasmic polyhedrosis virus polyhedrin in

- 815 insect cells by using a baculovirus expression vector, and its assembly into
816 polyhedra, *Journal of General Virology* 74 (1) (1993) 99–102. doi:10.
817 1099/0022-1317-74-1-99.
- 818 [20] S. H. Green, E. Bailey, Q. Wang, R. L. Davis, The Trk A, B, C's of
819 Neurotrophins in the Cochlea., *Anatomical record (Hoboken, N.J. : 2007)*
820 295 (11) (2012) 1877–1895. doi:10.1002/ar.22587.
- 821 [21] I. Meyvantsson, D. J. Beebe, Cell culture models in microfluidic systems,
822 *Annual Review of Analytical Chemistry* 1 (1) (2008) 423–449. doi:10.
823 1146/annurev.anchem.1.031207.113042.
- 824 [22] Z.-J. Guo, M.-H. Yu, X.-Y. Dong, W.-L. Wang, T. Tian, X.-Y. Yu, X.-D.
825 Tang, Protein composition analysis of polyhedra matrix of *Bombyx mori*
826 nucleopolyhedrovirus (BmNPV) showed powerful capacity of polyhedra to
827 encapsulate foreign proteins., *Scientific reports* 7 (1) (2017) 8768. doi:
828 10.1038/s41598-017-08987-8.
- 829 [23] A. J. Matsuoka, Z. A. Sayed, N. Stephanopoulos, E. J. Berns, A. R. Wad-
830 hwani, Z. D. Morrissey, D. M. Chadly, S. Kobayashi, A. N. Edelbrock,
831 T. Mashimo, C. A. Miller, T. L. McGuire, S. I. Stupp, J. A. Kessler,
832 Creating a stem cell niche in the inner ear using self-assembling peptide
833 amphiphiles., *Plos One* 12 (12) (2017) e0190150. doi:10.1371/journal.
834 pone.0190150.
- 835 [24] A. J. Matsuoka, Z. D. Morrissey, C. Zhang, K. Homma, A. Belmadani,
836 C. A. Miller, D. M. Chadly, S. Kobayashi, A. N. Edelbrock, M. Tanaka-
837 Matakatsu, D. S. Whitlon, L. Lyass, T. L. McGuire, S. I. Stupp, J. A.
838 Kessler, Directed Differentiation of Human Embryonic Stem Cells Toward
839 Placode-Derived Spiral Ganglion-Like Sensory Neurons, *Stem Cells Trans-
840 lational Medicine* 6 (2017) 923–936. doi:10.1002/sctm.16-0032.
- 841 [25] H. Al-Ali, S. R. Beckerman, J. L. Bixby, V. P. Lemmon, In vitro models
842 of axon regeneration, *Experimental Neurology* 287 (Pt 3) (2017) 423–434.
843 doi:10.1016/j.expneurol.2016.01.020.

- 844 [26] U. K. Laemmli, Cleavage of structural proteins during the assembly of
845 the head of bacteriophage T4., *Nature* 227 (5259) (1970) 680–685. doi:
846 10.1038/227680a0.
- 847 [27] A. L. Mandel, H. Ozdener, V. Utermohlen, Identification of pro- and mature
848 brain-derived neurotrophic factor in human saliva., *Archives of oral biology*
849 54 (7) (2009) 689–695. doi:10.1016/j.archoralbio.2009.04.005.
- 850 [28] C. A. Schneider, W. S. Rasband, K. W. Eliceiri, NIH Image to ImageJ:
851 25 years of image analysis, *Nature Methods* 9 (7) (2012) 671–675. arXiv:
852 arXiv:1011.1669v3, doi:10.1038/nmeth.2089.
- 853 [29] R. W. Burry, Controls for immunocytochemistry: an update., *The journal*
854 *of histochemistry and cytochemistry : official journal of the Histochemistry*
855 *Society* 59 (1) (2011) 6–12. doi:10.1369/jhc.2010.956920.
- 856 [30] M. B. Mazalan, M. A. B. Ramlan, J. H. Shin, T. Ohashi, Effect of geomet-
857 ric curvature on collective cell migration in tortuous microchannel devices,
858 *Micromachines* 11 (7) (2020) 1–17. doi:10.3390/MI11070659.
- 859 [31] F. Xu, T. Beyazoglu, E. Hefner, U. A. Gurkan, U. Demirci, Automated
860 and adaptable quantification of cellular alignment from microscopic images
861 for tissue engineering applications, *Tissue Engineering - Part C: Methods*
862 17 (6) (2011) 641–649. doi:10.1089/ten.tec.2011.0038.
- 863 [32] E. Batschelet, *Circular Statistics in Biology (Mathematics in Biology Series)*,
864 1st Edition, Academic Press, New York, NY, 1981.
- 865 [33] P. Berens, M. J. Velasco, CircStat for Matlab: Toolbox for circular statistics
866 with Matlab, Max–Planck–Institut f ur biologische Kybernetik, Technical
867 Report No. 184 31 (10) (2009) 1–21. doi:doi:10.18637/jss.v031.i10.
- 868 [34] M. Pool, J. Thiemann, A. Bar-Or, A. E. Fournier, NeuriteTracer: A novel
869 ImageJ plugin for automated quantification of neurite outgrowth, *Jour-*
870 *nal of Neuroscience Methods* 168 (1) (2008) 134–139. doi:10.1016/j.
871 jneumeth.2007.08.029.

- 872 [35] E. Meijering, M. Jacob, J.-C. F. Sarria, P. Steiner, H. Hirling, M. Unser,
873 Design and validation of a tool for neurite tracing and analysis in fluo-
874 rescence microscopy images., *Cytometry. Part A : the journal of the In-*
875 *ternational Society for Analytical Cytology* 58 (2) (2004) 167–176. doi:
876 [10.1002/cyto.a.20022](https://doi.org/10.1002/cyto.a.20022).
- 877 [36] M. Anniko, W. Arnold, T. Stigbrand, A. Strom, The Human Spiral Gan-
878 glion, *ORL* 57 (1995) 68–77.
- 879 [37] S. van der Walt, S. C. Colbert, G. Varoquaux, The NumPy Array: A
880 Structure for Efficient Numerical Computation, *Computing in Science En-*
881 *gineering* 13 (2) (2011) 22–30. doi:[10.1109/MCSE.2011.37](https://doi.org/10.1109/MCSE.2011.37).
- 882 [38] J. D. Hunter, Matplotlib: A 2D Graphics Environment, *Computing in*
883 *Science Engineering* 9 (3) (2007) 90–95. doi:[10.1109/MCSE.2007.55](https://doi.org/10.1109/MCSE.2007.55).
- 884 [39] P. Virtanen, R. Gommers, T. E. Oliphant, M. Haberland, T. Reddy,
885 D. Cournapeau, E. Burovski, P. Peterson, W. Weckesser, J. Bright, S. J.
886 van der Walt, M. Brett, J. Wilson, K. J. Millman, N. Mayorov, A. R. J.
887 Nelson, E. Jones, R. Kern, E. Larson, C. J. Carey, I. Polat, Y. Feng,
888 E. W. Moore, J. VanderPlas, D. Laxalde, J. Perktold, R. Cimrman, I. Hen-
889 riksen, E. A. Quintero, C. R. Harris, A. M. Archibald, A. H. Ribeiro,
890 F. Pedregosa, P. van Mulbregt, SciPy 1.0: fundamental algorithms for
891 scientific computing in Python., *Nature methods* 17 (3) (2020) 261–272.
892 doi:[10.1038/s41592-019-0686-2](https://doi.org/10.1038/s41592-019-0686-2).
- 893 [40] P. Berens, CircStat : A MATLAB Toolbox for Circular Statistics , *Journal*
894 *of Statistical Software* 31 (10). doi:[10.18637/jss.v031.i10](https://doi.org/10.18637/jss.v031.i10).
- 895 [41] M. Tuncel, H. S. Sürütü, K. M. Erbil, A. Konan, Formation of the cochlear
896 nerve in the modiolus of the guinea pig and human cochleae., *Archives of*
897 *medical research* 36 (5) (2005) 436–40. doi:[10.1016/j.arcmed.2005.02.003](https://doi.org/10.1016/j.arcmed.2005.02.003).

- 899 [42] B. Küçük, K. Abe, T. Ushiki, Y. Inuyama, S. Fukuda, Kazuo Ishikawa,
900 Microstructures of the Bony Modiolus in the Human Cochlea : A Scanning
901 Electron Microscopic Study, *Journal of Electron Microsc* 40 (40) (1991)
902 193–197.
- 903 [43] O. Levenspiel, *Chemical Reaction Engineering*, 3rd Edition, John Wiley
904 and Sons, Inc., New York, NY, 1999.
- 905 [44] M. Stroh, W. R. Zipfel, R. M. Williams, S. C. Ma, W. W. Webb, W. M.
906 Saltzman, Multiphoton microscopy guides neurotrophin modification with
907 poly(ethylene glycol) to enhance interstitial diffusion, *Nature Materials*
908 3 (7) (2004) 489–494. doi:10.1038/nmat1159.
- 909 [45] S. Axler, *Linear Algebra Done Right*, 3rd Edition, Springer Publishing,
910 New York, NY, 2015.
- 911 [46] J. Crank, *The mathematics of Diffusion*, 2nd Edition, Oxford University
912 Press, London, UK, 1979.
- 913 [47] K. M. Keefe, I. S. Sheikh, G. M. Smith, Targeting Neurotrophins to Specific
914 Populations of Neurons: NGF, BDNF, and NT-3 and Their Relevance
915 for Treatment of Spinal Cord Injury., *International journal of molecular*
916 sciences
- 18 (3). doi:10.3390/ijms18030548.
- 917 [48] B. I. Awad, M. A. Carmody, M. P. Steinmetz, Potential role of growth
918 factors in the management of spinal cord injury., *World Neurosurgery* 83 (1)
919 (2015) 120–131. doi:10.1016/j.wneu.2013.01.042.
- 920 [49] E. R. n. Hollis, M. H. Tuszyński, Neurotrophins: potential therapeutic tools
921 for the treatment of spinal cord injury., *Neurotherapeutics : the journal of*
922 *the American Society for Experimental NeuroTherapeutics* 8 (4) (2011)
923 694–703. doi:10.1007/s13311-011-0074-9.
- 924 [50] A. H. Nagahara, B. R. Wilson, I. Ivasyk, I. Kovacs, S. Rawalji, J. R.
925 Bringas, P. J. Piviroto, W. S. Sebastian, L. Samaranch, K. S. Bankiewicz,

- 926 M. H. Tuszynski, MR-guided delivery of AAV2-BDNF into the entorhi-
927 nal cortex of non-human primates., *Gene therapy* 25 (2) (2018) 104–114.
928 [doi:10.1038/s41434-018-0010-2](https://doi.org/10.1038/s41434-018-0010-2).
- 929 [51] S. D. Croll, C. Suri, D. L. Compton, M. V. Simmons, G. D. Yan-
930 copoulos, R. M. Lindsay, S. J. Wiegand, J. S. Rudge, H. E. Scharfman,
931 Brain-derived neurotrophic factor transgenic mice exhibit passive avoid-
932 ance deficits, increased seizure severity and in vitro hyperexcitability in
933 the hippocampus and entorhinal cortex., *Neuroscience* 93 (4) (1999) 1491–
934 1506. [doi:10.1016/s0306-4522\(99\)00296-1](https://doi.org/10.1016/s0306-4522(99)00296-1).
- 935 [52] A. Dravid, S. Parittotokkaporn, Z. Aqrawe, S. J. O'Carroll, D. Svirskis,
936 Determining Neurotrophin Gradients in Vitro to Direct Axonal Outgrowth
937 following Spinal Cord Injury, *ACS Chemical Neuroscience* 11 (2) (2020)
938 121–132. [doi:10.1021/acscchemneuro.9b00565](https://doi.org/10.1021/acscchemneuro.9b00565).
- 939 [53] T. Yamagata, J. M. Miller, M. Ulfendahl, N. P. Olivius, R. A. Altschuler,
940 I. Pyykkö, G. Bredberg, Delayed neurotrophic treatment preserves nerve
941 survival and electrophysiological responsiveness in neomycin-deafened
942 guinea pigs., *Journal of neuroscience research* 78 (1) (2004) 75–86. [doi:
943 10.1002/jnr.20239](https://doi.org/10.1002/jnr.20239).
- 944 [54] M. P. Zanin, M. Hellstr??m, R. K. Shepherd, A. R. Harvey, L. N. Gillespie,
945 Development of a cell-based treatment for long-term neurotrophin expres-
946 sion and spiral ganglion neuron survival, *Neuroscience* 277 (2014) 690–699.
947 [doi:10.1016/j.neuroscience.2014.07.044](https://doi.org/10.1016/j.neuroscience.2014.07.044).
- 948 [55] M. Seyyedi, L. Viana, J. J. Nadol, Within-subject comparison of word
949 recognition and spiral ganglion cell count in bilateral cochlear implant
950 recipients, *Otol Neurotol* 35 (8) (2014) 1446–1450. [doi:10.1097/MAO.
951 000000000000443.Within-Subject](https://doi.org/10.1097/MAO.000000000000443).
- 952 [56] A. Henriques, C. Pitzer, A. Schneider, Neurotrophic growth factors for the
953 treatment of amyotrophic lateral sclerosis: where do we stand?, *Frontiers
954 in neuroscience* 4 (2010) 32. [doi:10.3389/fnins.2010.00032](https://doi.org/10.3389/fnins.2010.00032).

- 955 [57] J. F. Poduslo, G. L. Curran, Permeability at the blood-brain and
956 blood-nerve barriers of the neurotrophic factors: NGF, CNTF, NT-3,
957 BDNF, Molecular Brain Research 36 (2) (1996) 280–286. doi:10.1016/
958 0169-328X(95)00250-V.
- 959 [58] T. Sakane, W. M. Pardridge, Carboxyl-directed pegylation of brain-derived
960 neurotrophic factor markedly reduces systemic clearance with minimal loss
961 of biologic activity (1997). doi:10.1023/A:1012117815460.
- 962 [59] R. G. Soderquist, E. D. Milligan, E. M. Sloane, J. A. Harrison, K. K.
963 Douvas, J. M. Potter, T. S. Hughes, R. A. Chavez, K. Johnson, L. R.
964 Watkins, M. J. Mahoney, PEGylation of brain-derived neurotrophic factor
965 for preserved biological activity and enhanced spinal cord distribution.,
966 Journal of biomedical materials research. Part A 91 (3) (2009) 719–729.
967 doi:10.1002/jbm.a.32254.
- 968 [60] M. Sasi, B. Vignoli, M. Canossa, R. Blum, Neurobiology of local and inter-
969 cellular BDNF signaling, Pflugers Archiv : European journal of physiology
970 469 (5-6) (2017) 593–610. doi:10.1007/s00424-017-1964-4.
- 971 [61] X. Li, Y. Su, S. Liu, L. Tan, X. Mo, S. Ramakrishna, Encapsulation
972 of proteins in poly(l-lactide-co-caprolactone) fibers by emulsion electro-
973 spinning, Colloids and Surfaces B: Biointerfaces 75 (2) (2010) 418–424.
974 doi:10.1016/j.colsurfb.2009.09.014.
- 975 [62] E. E. L. Swan, M. Peppi, Z. Chen, K. M. Green, J. E. Evans, M. J.
976 McKenna, M. J. Mescher, S. G. Kujawa, W. F. Sewell, Proteomics analysis
977 of perilymph and cerebrospinal fluid in mouse., The Laryngoscope 119 (5)
978 (2009) 953–958. doi:10.1002/lary.20209.
- 979 [63] T. Numakawa, S. Suzuki, E. Kumamaru, N. Adachi, M. Richards,
980 H. Kunugi, BDNF function and intracellular signaling in neurons, Histology
981 and Histopathology 25 (2) (2010) 237–258. doi:10.14670/HH-25.237.

- 982 [64] C. Gentile, Engineering of Spheroids for Stem Cell Technology, Current
983 Stem Cell Research & Therapy 11 (2016) 652–665. doi:10.2174/
984 1574888x10666151001114848.
- 985 [65] H. Berg, Random Walks in Biology, Princeton Universtiy Press, Prinston,
986 NJ, 1983.
- 987 [66] H. Li, F. Edin, H. Hayashi, O. Gudjonsson, N. Danckwardt-Lillies, H. En-
988 gqvist, H. Rask-Andersen, W. Xia, Guided growth of auditory neurons:
989 Bioactive particles towards gapless neural electrode interface, Biomaterials
990 122 (2017) 1–9. doi:10.1016/j.biomaterials.2016.12.020.
- 991 [67] J. Schulze, H. Staeker, D. Wedekind, T. Lenarz, A. Warnecke, Expression
992 pattern of brain-derived neurotrophic factor and its associated receptors:
993 Implications for exogenous neurotrophin application., Hearing Research 413
994 (2020) 108098. doi:10.1016/j.heares.2020.108098.